



HAL
open science

A conservative Immersed Boundary method for an inviscid compressible flow coupled with a fragmenting structure

Maria Adela Puscas, Laurent Monasse, Alexandre Ern, Christian Tenaud,
Christian Mariotti

► **To cite this version:**

Maria Adela Puscas, Laurent Monasse, Alexandre Ern, Christian Tenaud, Christian Mariotti. A conservative Immersed Boundary method for an inviscid compressible flow coupled with a fragmenting structure. 2014. hal-01071619v1

HAL Id: hal-01071619

<https://hal.science/hal-01071619v1>

Submitted on 6 Oct 2014 (v1), last revised 1 Feb 2015 (v2)

HAL is a multi-disciplinary open access archive for the deposit and dissemination of scientific research documents, whether they are published or not. The documents may come from teaching and research institutions in France or abroad, or from public or private research centers.

L'archive ouverte pluridisciplinaire **HAL**, est destinée au dépôt et à la diffusion de documents scientifiques de niveau recherche, publiés ou non, émanant des établissements d'enseignement et de recherche français ou étrangers, des laboratoires publics ou privés.

A conservative Immersed Boundary method for an inviscid compressible flow coupled with a fragmenting structure

Maria Adela Puscas^{1, 2, 3}, Laurent Monasse¹, Alexandre Ern¹, Christian Tenaud³,
Christian Mariotti²

¹ Université Paris-Est, CERMICS (ENPC),
77455 Marne la Vallée cedex, France

email: {puscasa, ern, monassel}@cermics.enpc.fr

² CEA-DAM-DIF 91297 Arpaçon, France

email: {adela.puscas, christian.mariotti}@cea.fr

³ LIMSI-CNRS, 91403 Orsay, France

email: {adela.puscas, christian.tenaud}@limsi.fr

ABSTRACT

We present a conservative method for the interaction between an inviscid compressible flow and a fragmenting structure. On the fluid side, we consider an inviscid Euler fluid in conservative form discretized using a Finite Volume method combining Lax-Friedrichs fluxes in fluid cells located near the opening fractures when the density and pressure are zero or very low with high-order monotonicity-preserving fluxes elsewhere. On the solid side, we consider a fragmenting solid discretized with a Discrete Element method where fragmentation occurs through the breaking of links between the particles discretizing the solid. The fluid-solid coupling is achieved by an Immersed Boundary technique through the modification of the Finite Volume fluxes in the vicinity of the solid. A time explicit approach is used for the computation of the energy and momentum transfer between the solid and the fluid.

Key Words: Fluid-structure interaction, Finite Volume, Immersed Boundary, Conservative method, Fragmenting structure

1 Introduction

In the present work, we are interested in the interaction of a shocked fluid with a fragmenting structure. The characteristic time scales of these phenomena are extremely short. The driving effect is the fluid overpressure, and viscous effects play a lesser role in the dynamics of system, so that we consider an inviscid fluid. An important class of methods for fluid-structure interaction hinges on a partitioned approach, where the fluid and the solid equations are solved separately, and an interface module is used to exchange information between the fluid and the solid solvers. Two main types of methods have been developed in this context: Arbitrary Lagrangian-Eulerian (ALE) methods [9, 19] and fictitious domain methods [5, 11, 12, 14, 15, 27, 36]. The ALE method deforms the fluid domain in order to follow the movement of the structure. This method hinges on a mesh fitting the solid boundaries, and this often involves possibly costly remeshing of the fluid domain when the solid goes through large displacements and especially fragmentation. Fictitious domain methods work on a fixed fluid grid. The solid is superimposed to the fluid grid, and additional terms are introduced in the fluid solver to impose the fluid boundary conditions at the solid boundary. Such methods can treat large displacements of the solid and changes in the topology of the fluid domain without remeshing. Various types of fictitious domain methods have been proposed. In particular, Conservative Immersed Boundary methods [3, 13, 17, 18, 26, 28, 29, 31] have been developed for elliptic problems and compressible fluids, so that the spatial discretization conserves mass, momentum, and energy.

Coupling fluids with fragmenting structures has already been addressed in the literature. An Immersed Boundary approach for a fluid interacting with a fracturing and fragmenting thin shell was developed in [2, 6]. The method couples a Lagrangian fragmenting thin shell discretized by a Finite Element method and an Eulerian fluid flow discretized by a Finite Volume method on a Cartesian grid. This method uses a Level Set approach to track the immersed solid surface, and a Ghost Fluid method to impose the boundary conditions at the fluid-structure interface. The thin shell fracture criterion is based on a

cohesive interface method and uses pre-fractured elements to model the fracture, so that the knowledge of where the fracture will occur is required. An Immersed Particle method [34] was used in [30] for the interaction of a compressible fluid with a fragmenting thin shell, without a priori knowledge of the fracture location. The fracture is modelled by a cracking particle method using a local partition of unity. This method treats both fluid and structure by meshfree particle methods, and the solid is immersed in the fluid. The fluid model is Lagrangian and for very large deformation situations, a reinitialization of the fluid particles is necessary (defaulting energy conservation). Another Immersed Boundary approach for the interaction between a compressible flow and a fragmenting thin shell was developed in [20], also without a priori knowledge of the fracture location. The fluid is discretized using a Finite Volume method. The method for the fragmenting structure combines an Extended Finite Element method (X-FEM) [8, 33] with cohesive law and element deletion.

In the present work, we develop a conservative method for the three-dimensional interaction between an inviscid fluid and a fragmenting structure. On the fluid side, we consider an inviscid Euler fluid in conservative form discretized using a high-order monotonicity-preserving Finite Volume method with directional operator splitting [4]. On the solid side, we consider a fragmenting solid discretized with the Discrete Element method [25]. This method discretized the solid using particles, and each particle is governed by the classical equations of mechanics. The particles interact through forces and torques. The Discrete Element method treats naturally fragmentation by breaking links between particles and does not need remeshing of the domain. A conservative time-explicit coupling algorithm between an inviscid fluid and a three-dimensional rigid or deformable solid without fragmentation was developed in [28, 29], using a conservative Immersed Boundary technique. The present work extends the coupling method of [28, 29] to include the fragmentation of the solid. The meaning of the word "conservative" is twofold. First, we employ a cut-cell modification of the Finite Volume method, which ensures exact conservation of mass, momentum, and energy quantities in the fluid. Second, we verify that the exchange of fluid and solid momentum and energy through their interface is balanced. As the solid time integration scheme is symplectic, it is not conservative but preserves a discrete energy (which is a close approximation of the local energy). The coupled discrete system is therefore not exactly conservative, but we show numerically that our strategy gives excellent conservation results for the energy.

In the Discrete Element method, the fracture propagates element by element using a fracture criterion defined at the contact faces between particles. The coupling method is independent of the breaking criterion used in the solid solver in order to break the link between particles. In the present work, we focus on the feasibility study of the coupling method to deal with fragmentation, so that it is sufficient at this stage to employ a simple model for the breaking criterion based on a maximal elongation of particles link. During the fragmentation process, vacuum between solid particles can occur due to internal solid fragmentation and to the fact that the velocity of the crack propagation can be larger than the speed of sound in the fluid. This leads to fluid cells where the fluid pressure and the density are zero or very low. We consider the Lax–Friedrichs numerical flux near the vacuum area in order to avoid division by pressure or density. The Lax–Friedrichs flux is able to compute a stable approximation to the Riemann problem in the presence of vacuum [35]. Away from the vacuum, the high-order flux from [4] is used. Furthermore, the coupling algorithm is based on an explicit time-marching procedure. The algorithm does not require remeshing and allows fluid to pass through the opened areas of the structure without any a priori knowledge of where fragmentation occurs. The method deals with three-dimensional solids, and as in the case without fragmentation, the method yields conservation of mass, momentum, and energy of the system. One limitation of the present method is that it does not take into account the possible contact between particles during the ballistic flight after fragmentation.

The paper is organized as follows. In Section 2, we briefly set the notation and recall the coupling method without solid fragmentation. In Section 3, we present the conservative coupling method with fragmentation. In Section 4, we discuss numerical results. Finally, conclusions are drawn in Section 5.

2 Coupling without fragmentation

2.1 Fluid discretization

The inviscid compressible flow is modelled by the Euler equations. The equations are written in conservative form expressing conservation of mass, momentum, and energy as follows:

$$\frac{\partial}{\partial t}U + \frac{\partial}{\partial x}F(U) + \frac{\partial}{\partial y}G(U) + \frac{\partial}{\partial z}H(U) = 0, \quad (1)$$

where $U = (\rho, \rho u, \rho v, \rho w, \rho E)^t$ with ρ the mass density, p the pressure, (u, v, w) the Cartesian components of the velocity vector \vec{u} , and E the total energy. The pressure is modelled by the state equation of a perfect gas: $p = \rho(\gamma - 1)(E - \frac{1}{2}(u^2 + v^2 + w^2))$, $\gamma = 1.4$ being the ratio of specific heats, assumed to be constant. The flux functions are given by

$$F(U) = \begin{pmatrix} \rho u \\ \rho u^2 + p \\ \rho uv \\ \rho uw \\ (\rho E + p)u \end{pmatrix}, \quad G(U) = \begin{pmatrix} \rho v \\ \rho v^2 + p \\ \rho vw \\ \rho vw \\ (\rho E + p)v \end{pmatrix}, \quad H(U) = \begin{pmatrix} \rho w \\ \rho w^2 + p \\ \rho vw \\ \rho w^2 + p \\ (\rho E + p)w \end{pmatrix},$$

2.1.1 Fluid grid

In Immersed Boundary methods, the solid is superimposed to the fluid grid. As a result, some cells of the fluid grid are masked by the solid and are named ‘‘solid cells’’, some others are completely included in the flow domain and are called ‘‘fluid cells’’, and the remaining ones are intersected by the surface of the solid and are referred to as ‘‘cut cells’’ (see Fig. 1). We denote by $\Omega_{\text{Solid}}(t)$ the solid domain and by $\Omega_{\text{Fluid}}(t)$ the fluid domain.

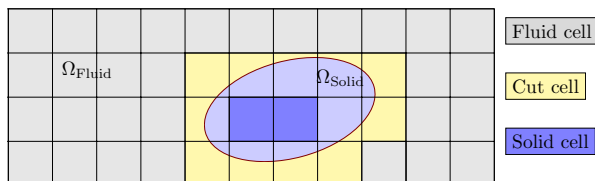


Figure 1: Solid superimposed to the fluid grid

We consider a Cartesian fluid grid, and we denote with integer subscripts i, j, k quantities related to the center of cells and with half-integer subscripts quantities related to the center of faces of cells. For instance, the interface between cells $C_{i,j,k}$ and $C_{i+1,j,k}$ is denoted by $\partial C_{i+\frac{1}{2},j,k}$. The relevant geometric quantities describing the intersection between the moving solid and the cut cell $C_{i,j,k}$ are:

- The **volume fraction** $0 \leq \Lambda_{i,j,k}^n \leq 1$ occupied by the solid in the cell $C_{i,j,k}$ at time t^n .
- The **side area fractions** $0 \leq \lambda_{i\pm\frac{1}{2},j,k}^n, \lambda_{i,j,\pm\frac{1}{2},k}^n, \lambda_{i,j,k\pm\frac{1}{2}}^n \leq 1$ of each cell face at time t^n .

The three-dimensional geometric algorithms used for the detection of the cut cells and the computation of the intersection between the solid and the fluid grid are described in [29].

In the explicit Finite Volume scheme, the time-step, denoted by Δt , is subjected to the following CFL stability condition:

$$\Delta t < \min_{i,j,k} \left(\frac{\Delta x_{i,j,k}}{|\vec{u}_{i,j,k}| + c_{i,j,k}} \right), \quad (2)$$

where c is the speed of sound in the fluid, $c^2 = \frac{\gamma p}{\rho}$. The time-step is taken constant for simplicity. We introduce the discrete times $t^n = n\Delta t$, for all $n \geq 0$.

2.1.2 Fluid cells

Let $C_{i,j,k}$ be a fluid cell ($\Lambda_{i,j,k}^{n+1} = 0$) of size $(\Delta x_{i,j,k}, \Delta y_{i,j,k}, \Delta z_{i,j,k})$. The Finite Volume formulation takes the form

$$U_{i,j,k}^{n+1} = U_{i,j,k}^n + \Delta t \Phi_{i,j,k}^n \text{ fluid}, \quad (3)$$

with the flux $\Phi_{i,j,k}^n$ fluid given by

$$\Phi_{i,j,k}^n \text{ fluid} = \frac{F_{i-1/2,j,k}^n - F_{i+1/2,j,k}^n}{\Delta x_{i,j,k}} + \frac{G_{i,j-1/2,k}^n - G_{i,j+1/2,k}^n}{\Delta y_{i,j,k}} + \frac{H_{i,j,k-1/2}^n - H_{i,j,k+1/2}^n}{\Delta z_{i,j,k}}, \quad (4)$$

where $U_{i,j,k}^n$ is the numerical approximation of the exact solution over the cell $C_{i,j,k}$ at time t^n , and $F_{i\pm 1/2,j,k}^n$, $G_{i,j\pm 1/2,k}^n$, $H_{i,j,k\pm 1/2}^n$ are numerical fluxes approximating the time-average of the corresponding physical flux over the time interval $[t^n, t^{n+1}]$ and evaluated at $\partial C_{i\pm 1/2,j,k}$, $\partial C_{i,j\pm 1/2,k}$, and $\partial C_{i,j,k\pm 1/2}$, respectively. We use the unidimensional One-Step Monotonicity-Preserving (OSMP) high-order scheme [4]. This scheme is derived using a coupled space-time Lax–Wendroff approach, where the formal order of accuracy in the scalar case can be set to an arbitrary order. In the present work, we use order 11. The extension to the multidimensional case is made with a directional operator splitting consisting in solving alternately the one-dimensional problem in each direction [32]. Let L_x , L_y , L_z denote the operators corresponding to the integration over a time-step Δt in the x , y , and z directions, respectively. For instance,

$$L_x(\Delta t)W = W - \Delta t \left(\frac{F_{i+\frac{1}{2},j,k}(W) - F_{i-\frac{1}{2},j,k}(W)}{\Delta x} \right).$$

Then, we define, for example

$$U_{i,j,k}^{n+1} = L_x(\Delta t)L_y(\Delta t)L_z(\Delta t)U_{i,j,k}^n.$$

Formal second-order time accuracy is recovered every six time-steps (corresponding to all L_x , L_y , and L_z permutations) if the directional operators do not commute [4]. Finally, we denote by \bar{p}_x^n , \bar{p}_y^n , and \bar{p}_z^n the pressures used in the application of the operators L_x , L_y , and L_z respectively. These quantities are used in the fluid-structure coupling.

2.1.3 Cut cells

We take into account the position of the solid in the fluid domain by modifying (3) in the cut cells. In a cut cell $C_{i,j,k}$ ($0 < \Lambda_{i,j,k}^{n+1} < 1$), we consider the following approximation of (1):

$$\left(1 - \Lambda_{i,j,k}^{n+1}\right)U_{i,j,k}^{n+1} = \left(1 - \Lambda_{i,j,k}^{n+1}\right)U_{i,j,k}^n + \Delta t \Phi_{i,j,k}^n \text{ fluid} + \Delta t \Phi_{i,j,k}^n \text{ solid} + \Delta U_{i,j,k}^{n,n+1}, \quad (5)$$

where the fluid flux $\Phi_{i,j,k}^n$ fluid is now given by (compare with (4), see [29] for details)

$$\begin{aligned} \Phi_{i,j,k}^n \text{ fluid} = & \frac{\left(1 - \lambda_{i-\frac{1}{2},j,k}^{n+1}\right)F_{i-\frac{1}{2},j,k}^n - \left(1 - \lambda_{i+\frac{1}{2},j,k}^{n+1}\right)F_{i+\frac{1}{2},j,k}^n}{\Delta x_{i,j,k}} \\ & + \frac{\left(1 - \lambda_{i,j-\frac{1}{2},k}^{n+1}\right)G_{i,j-\frac{1}{2},k}^n - \left(1 - \lambda_{i,j+\frac{1}{2},k}^{n+1}\right)G_{i,j+\frac{1}{2},k}^n}{\Delta y_{i,j,k}} \\ & + \frac{\left(1 - \lambda_{i,j,k-\frac{1}{2}}^{n+1}\right)H_{i,j,k-\frac{1}{2}}^n - \left(1 - \lambda_{i,j,k+\frac{1}{2}}^{n+1}\right)H_{i,j,k+\frac{1}{2}}^n}{\Delta z_{i,j,k}}. \end{aligned} \quad (6)$$

The solid flux $\Phi_{i,j,k}^n$ solid resulting from the presence of the solid boundaries in the cut cell and the swept amount $\Delta U_{i,j,k}^{n,n+1}$ are detailed in Section 2.3.

This approach can involve “small cut-cells” in which the solid volume fraction is greater than 0.5. In order to ensure the CFL stability condition of the fluid scheme on these cells, the time-step should be decreased to an unacceptably small value:

$$\Delta t < \min_{i,j,k} \left(\frac{(1 - \Lambda_{i,j,k})\Delta x_{i,j,k}}{|\vec{u}_{i,j,k}| + c_{i,j,k}} \right),$$

Several approaches are available to ensure stability without a drastic reduction of the time-step and at the same time preserve the conservation properties of the scheme. For example, [13] suggests merging small cut-cells with a neighboring fluid cell. Since it is not always possible to find for each small cut-cell a neighboring fluid cell, a conservative mixing of the cut cell with a fluid cell, found in the direction of the outward normal to the solid boundary present in the cut cell is proposed in [18]. Let p be a small cut-cell and let g be the fluid cell in question ($\Lambda_g = 0$). The mixing procedure consists in defining the following exchange terms:

$$E_{pg} = \frac{1}{(2 - \Lambda_p)}(U_g - U_p), \quad E_{gp} = \frac{(1 - \Lambda_p)}{(2 - \Lambda_p)}(U_p - U_g),$$

and setting $U_p \leftarrow U_p + E_{pg}$, $U_g \leftarrow U_g + E_{gp}$. The mixing procedure is conservative since $(1 - \Lambda_p)E_{pg} + E_{gp} = 0$.

2.1.4 Solid cells

The stencil used in the OSMP flux function can overlap with the solid. Near the solid, the states needed to calculate the fluid fluxes may be located in cells completely occupied by the solid (solid cells, $\Lambda = 1$). In this situation, we define in these solid cells a fictitious state from the states associated with the mirror cells relatively to the fluid-solid interface (see [29]).

2.2 Solid discretization

The deformable moving solid is discretized by the Discrete Element method using a finite number of rigid particles (Fig. 2). Each particle is governed by the classical equations of mechanics. The particles interact through forces and torques. The expression of these forces and torques allows one to recover the macroscopic behavior of the solid [22, 25].

2.2.1 Forces and torques between particles

Various quantities are attached to a generic solid particle I , namely the mass m_I , the volume V_I and the free volume V_I^l , the position of the center of mass \vec{X}_I , the velocity of the center of mass \vec{V}_I , the rotation matrix \mathbf{Q}_I , the angular momentum matrix \mathbf{P}_I , and the principal moments of inertia I_I^i , $i \in \{1, 2, 3\}$. Let $\mathbf{D}_I = \text{diag}(d_I^1, d_I^2, d_I^3)$ with $d_I^i = \frac{1}{2}(I_I^1 + I_I^2 + I_I^3) - I_I^i$, $i \in \{1, 2, 3\}$. We denote by τ_I the neighbouring particles linked to particle I . Various quantities are attached to the link between the particle I and a neighbouring particle $J \in \tau_I$, namely the distance between these particles D_{IJ} , the contact surface S_{IJ} , the center of mass of the contact surface \vec{G}_{IJ} , the exterior normal vector at the contact surface \vec{n}_{IJ} , and the principal moments of the contact surface I_{IJ}^s and I_{IJ}^t . We also define two orthogonal vectors at the contact surface \vec{s}_{IJ} and \vec{t}_{IJ} forming an orthonormal basis with \vec{n}_{IJ} . \vec{X}_I^0 , D_{IJ}^0 , and \vec{n}_{IJ}^0 denote the initial values for \vec{X}_I , D_{IJ} , and \vec{n}_{IJ} respectively.

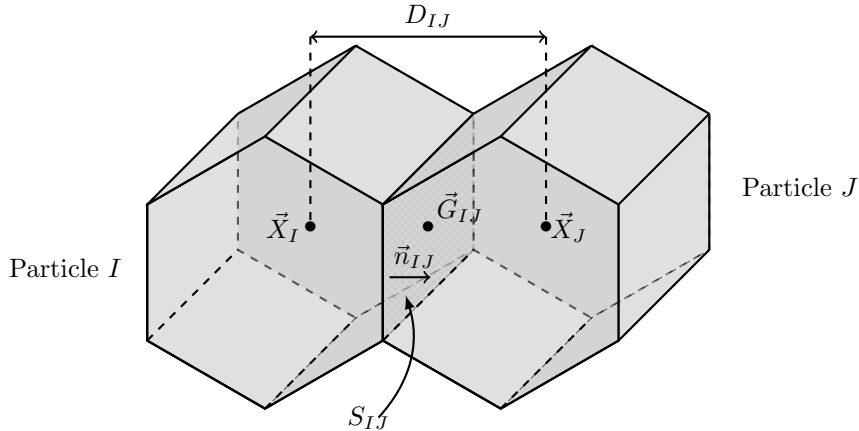


Figure 2: Solid discretization

Forces and torques between particles I and J are modelled by a linear elasticity behavior [22, 25]. The solid is characterised by the Young modulus E and by the Poisson ratio ν . The forces and torques between particles are derived from an Hamiltonian formulation. We briefly recall the expression of these forces and torques, for a detailed review see [22, 25]. The force between particles I and $J \in \tau_I$ is given by

$$\vec{F}_{IJ} = \frac{S_{IJ}}{D_{IJ}^0} \frac{E}{1+\nu} \vec{\Delta}u_{IJ} + S_{IJ} \frac{E\nu}{(1+\nu)(1-2\nu)} \varepsilon_{IJ}^v \left(\vec{n}_{IJ} + \frac{1}{D_{IJ}} \vec{\Delta}u_{IJ} - \frac{1}{D_{IJ}} (\vec{\Delta}u_{IJ} \cdot \vec{n}_{IJ}) \vec{n}_{IJ} \right),$$

where $\vec{\Delta}u_{IJ} = \vec{X}_I - \vec{X}_J + \mathbf{Q}_J \cdot \vec{X}_J^0 \vec{G}_{IJ} - \mathbf{Q}_I \cdot \vec{X}_I^0 \vec{G}_{IJ}$ is the displacement vector to the contact surface between I and J , and the volumetric deformation of the link between I and J , $\varepsilon_{IJ}^v = \varepsilon_I^v + \varepsilon_J^v$, is the sum of the volumetric deformation of I and J , where:

$$\varepsilon_I^v = \sum_{J \in \tau_I} \frac{1}{2} \frac{S_{IJ}}{V_I + 3 \frac{\nu}{1-2\nu} V_I^l} \vec{\Delta}u_{IJ} \cdot \vec{n}_{IJ}.$$

The torque between particles I and J is given by $\vec{\mathcal{M}}_{IJ} = \vec{\mathcal{M}}_{IJ}^t + \vec{\mathcal{M}}_{IJ}^f$, where $\vec{\mathcal{M}}_{IJ}^t$ denotes the torque of force \vec{F}_{IJ} with respect to the center of gravity of the interface \vec{G}_{IJ} :

$$\vec{\mathcal{M}}_{IJ}^t = \frac{S_{IJ}}{D_{IJ}^0} \frac{E}{1+\nu} \left(\mathbf{Q}_I \cdot \vec{X}_I^0 \vec{G}_{IJ} \right) \wedge \vec{\Delta}u_{IJ} + S_{IJ} \frac{E\nu}{(1+\nu)(1-2\nu)} \varepsilon_{IJ}^v \left(\mathbf{Q}_I \cdot \vec{X}_I^0 \vec{G}_{IJ} \right) \wedge \vec{n}_{IJ},$$

and $\vec{\mathcal{M}}_{IJ}^f$ denotes the flexion-torsion torque:

$$\vec{\mathcal{M}}_{IJ}^f = \frac{S_{IJ}}{D_{IJ}^0} (\alpha_n (\mathbf{Q}_I \cdot \vec{n}_{IJ}^0) \wedge (\mathbf{Q}_J \cdot \vec{n}_{IJ}^0) + \alpha_s (\mathbf{Q}_I \cdot \vec{s}_{IJ}) \wedge (\mathbf{Q}_J \cdot \vec{s}_{IJ}) + \alpha_t (\mathbf{Q}_I \cdot \vec{t}_{IJ}) \wedge (\mathbf{Q}_J \cdot \vec{t}_{IJ})).$$

The coefficients α_n , α_s , and α_t are chosen to recover the exact flexion and torsion of a beam:

$$\alpha_n = \frac{(1+2\nu)E}{4(1+\nu)S_{IJ}} (I_{IJ}^s + I_{IJ}^t), \quad \alpha_s = \frac{E}{4(1+\nu)S_{IJ}} ((3+2\nu)I_{IJ}^s - (1+2\nu)I_{IJ}^t), \quad \text{and} \quad \alpha_t = \frac{E}{4(1+\nu)S_{IJ}} ((3+2\nu)I_{IJ}^t - (1+2\nu)I_{IJ}^s).$$

2.2.2 Time integration scheme

The explicit time-integration scheme for the solid consists of the Verlet scheme for translation and the RATTLE scheme for rotation. For particle I , it takes the following form:

$$\vec{V}_I^{n+\frac{1}{2}} = \vec{V}_I^n + \frac{\Delta t}{2m_I} (\vec{F}_{I,\text{int}}^n + \vec{F}_{I,\text{fluid}}^n), \quad (7)$$

$$\vec{X}_I^{n+1} = \vec{X}_I^n + \Delta t \vec{V}_I^{n+\frac{1}{2}}, \quad (8)$$

$$\mathbf{P}_I^{n+\frac{1}{2}} = \mathbf{P}_I^n + \frac{\Delta t}{4} \mathbf{j} (\vec{\mathcal{M}}_{I,\text{int}}^n + \vec{\mathcal{M}}_{I,\text{fluid}}^n) \mathbf{Q}_I^n + \frac{\Delta t}{2} \mathbf{\Upsilon}_I^n \mathbf{Q}_I^n, \quad (9)$$

$$\mathbf{Q}_I^{n+1} = \mathbf{Q}_I^n + \Delta t \mathbf{P}_I^{n+\frac{1}{2}} \mathbf{D}_I^{-1}, \quad (10)$$

$$\vec{V}_I^{n+1} = \vec{V}_I^{n+\frac{1}{2}} + \frac{\Delta t}{2m_I} (\vec{F}_{I,\text{int}}^{n+1} + \vec{F}_{I,\text{fluid}}^n), \quad (11)$$

$$\mathbf{P}_I^{n+1} = \mathbf{P}_I^{n+\frac{1}{2}} + \frac{\Delta t}{4} \mathbf{j} (\vec{\mathcal{M}}_{I,\text{int}}^{n+1} + \vec{\mathcal{M}}_{I,\text{fluid}}^n) \mathbf{Q}_I^{n+1} + \frac{\Delta t}{2} \tilde{\mathbf{\Upsilon}}_I^{n+1} \mathbf{Q}_I^{n+1}, \quad (12)$$

where in (9), $\mathbf{\Upsilon}_I^n$ is a symmetric matrix such that $(\mathbf{Q}_I^{n+1})^t \mathbf{Q}_I^{n+1} = \mathbf{I}$, with \mathbf{I} the identity matrix in \mathbb{R}^3 , and in (12), $\tilde{\mathbf{\Upsilon}}_I^{n+1}$ is a symmetric matrix such that $(\mathbf{Q}_I^{n+1})^t \mathbf{P}_I^{n+1} \mathbf{D}_I^{-1} + \mathbf{D}_I^{-1} (\mathbf{P}_I^{n+1})^t \mathbf{Q}_I^{n+1} = \mathbf{0}$. The map $\mathbf{j} : \mathbb{R}^3 \rightarrow \mathbb{R}^{3 \times 3}$ is such that $\mathbf{j}(\vec{x})\vec{y} = \vec{x} \wedge \vec{y}$ for all $\vec{x}, \vec{y} \in \mathbb{R}^3$. The force $\vec{F}_{I,\text{int}}^n$ and the torque $\vec{\mathcal{M}}_{I,\text{int}}^n$ result from the interaction of particle I with its neighboring particles: $\vec{F}_{I,\text{int}}^n = \sum_{J \in \tau_I} \vec{F}_{IJ}^n$ and $\vec{\mathcal{M}}_{I,\text{int}}^n = \sum_{J \in \tau_I} \vec{\mathcal{M}}_{IJ}^n$. The forces $\vec{F}_{I,\text{fluid}}^n$ and $\vec{\mathcal{M}}_{I,\text{fluid}}^n$ are respectively the fluid force and torque applied to the particle I , and are detailed in Section 2.3.

2.2.3 Time step constraint

The time-integration scheme for the solid being explicit, the time-step is restricted by a CFL stability condition. This condition states that the displacement of each solid particle I during one time-step should be less than the characteristic size of the particles, and the rotation during one time-step should be less than $\frac{\pi}{8}$, see [25]. In the case of coupling with fluid, an additional condition applies to the displacement of the solid, requiring it to be less than one fluid grid cell size in the course of the time-step, so that the solid boundary crosses at most one fluid grid cell per time-step.

2.2.4 Definition of fluid-solid interface

The particles have a polyhedral shape and are assumed to be star-shaped with respect to their center of mass, and their faces are assumed to be star-shaped with respect to their center of mass. We define the thickness of the solid particle as the radius of its largest inscribed sphere. We assume that the solid particles have a thickness larger than or equal to two fluid grid cells. The faces of the solid particles in contact with the fluid are collected in the set \mathfrak{F} . A generic element of \mathfrak{F} is denoted by \mathcal{F} and is called a wet solid face. The fluid-solid interface consists of all the wet solid faces. Owing to the movement of the solid, the wet solid faces are time-dependent sets in \mathbb{R}^3 , and we set $\mathcal{F}^n = \mathcal{F}(t^n)$ for all $n \geq 0$. For each wet solid face $\mathcal{F}(t)$, we consider its surface $A_{\mathcal{F}}(t)$ and its normal $\vec{\nu}_{\mathcal{F}}(t)$ (pointing from the solid to the fluid). As long as the solid deforms without fragmentation a continuous interface around the particle assembly is reconstructed as follows. A vertex a_i of the initial Discrete Element lattice belongs to one or more polyhedral particles. We define the mean vertex \bar{a}_i corresponding to a_i as the average of the positions of vertex a_i under the rigid body motion of each particle which this vertex belongs to. Since the vertices $(\bar{a}_i)_i$ do not remain coplanar in general, the reconstructed fluid-solid interface is the set of triangles supported by the center of mass of the polyhedral particle face and the mean vertices $(\bar{a}_i)_i$.

2.3 Fluid-solid time integration

The computational cost of the fluid and solid methods lies mainly in the evaluation of fluxes on the fluid side and of forces and torques on the solid side. Both methods being time-explicit, we use a coupling algorithm based on an explicit time-marching procedure. This is reasonable since, in particular, added mass effects are expected to play a minimal role in the present situations. At the beginning of the time-step from t^n to t^{n+1} , we know the state of the fluid U^n , the position and rotation of the solid particles $(\vec{X}_I^n, \mathbf{Q}_I^n)$, as well as the velocity of their center of mass and their angular momentum $(\vec{V}_I^n, \mathbf{P}_I^n)$. For the fluid, we need to compute, for each fluid grid cell $C_{i,j,k}$, the fluxes $F_{i\pm 1/2,j,k}^{n+\frac{1}{2}}$, $G_{i,j\pm 1/2,k}^{n+\frac{1}{2}}$, $H_{i,j,k\pm 1/2}^{n+\frac{1}{2}}$, the volume fractions $\Lambda_{i,j,k}^{n+1}$, the side area fractions $\lambda_{i\pm 1/2,j,k}^{n+1}$, $\lambda_{i,j\pm 1/2,k}^{n+1}$, $\lambda_{i,j,k\pm 1/2}^{n+1}$, the solid fluxes $\Phi_{i,j,k,\text{solid}}^n$, and the swept amount $\Delta U_{i,j,k}^{n+1}$. For the solid, we need to compute, for each solid particle I , the fluid forces $\vec{F}_{I,\text{fluid}}^{n+1}$ and the fluid torques $\vec{\mathcal{M}}_{I,\text{fluid}}^{n+1}$.

The solid flux for a fluid cut cell $C_{i,j,k}$ is given by

$$\Phi_{i,j,k,\text{solid}}^n = \frac{1}{V_{i,j,k}} \sum_{\{\mathcal{F}^n \in \mathfrak{F} \mid \mathcal{F}^{n+1} \cap C_{i,j,k} \neq \emptyset\}} \phi_{i,j,k,\mathcal{F}}^n, \quad (13)$$

where $V_{i,j,k}$ is the volume of $C_{i,j,k}$, and $\phi_{i,j,k,\mathcal{F}}^n$ is the solid flux attached to the wet solid face \mathcal{F}^n intersecting the cell $C_{i,j,k}$ at time t^{n+1} (as indicated by the notation $\mathcal{F}^{n+1} \cap C_{i,j,k} \neq \emptyset$). To facilitate the computation of the solid flux and of the swept amount, we subdivide each solid face \mathcal{F} into a set of triangles, called sub-faces and generically denoted by f (so that $\mathcal{F} = \cup f$), that are contained in one fluid grid cell (not necessary the same) at times t^n and t^{n+1} . We set $f^n = f(t^n)$ for all $n \geq 0$. The solid flux attached to the face \mathcal{F}^n is then decomposed as

$$\phi_{i,j,k,\mathcal{F}}^n = \sum_{\{f^n \in \mathcal{F}^n \mid f^n \subset C_{i,j,k}\}} \left(0, \Pi_{x,f}^n, \Pi_{y,f}^n, \Pi_{z,f}^n, \vec{V}_f^{n+\frac{1}{2}} \cdot \vec{\Pi}_f^n \right)^t,$$

where

$$\vec{\Pi}_f^n = \left(\int_{f^n} \bar{p}_x^n \nu_{x,f}^n, \int_{f^n} \bar{p}_y^n \nu_{y,f}^n, \int_{f^n} \bar{p}_z^n \nu_{z,f}^n \right)^t,$$

and $\vec{V}_f^{n+\frac{1}{2}} = \vec{V}^{n+\frac{1}{2}} + \vec{\Omega}^{n+\frac{1}{2}} \wedge (\vec{X}_f^n - \vec{X}^n)$ is the velocity of the center of mass of f^n , \vec{X}_f^n is the center of mass of f^n , while $\vec{V}^{n+\frac{1}{2}}$ and $\vec{\Omega}^{n+\frac{1}{2}}$ are, respectively, the average velocity and rotation velocity of the solid particle containing f . Furthermore, the swept amount is given by

$$\Delta U_{i,j,k}^{n,n+1} = \sum_{\{\mathcal{F}^n \in \mathfrak{F} \mid \mathcal{F}^{n+1} \cap C_{i,j,k} \neq \emptyset\}} \Delta U_{i,j,k,\mathcal{F}}^{n,n+1},$$

where the term $\Delta U_{i,j,k,\mathcal{F}}^{n,n+1}$ denotes the amount of U swept by the movement of the wet solid face \mathcal{F} during the time-step from t^n to t^{n+1} . We define an affine map $\Psi_{n,n+1}$ from \mathcal{F}^n to \mathcal{F}^{n+1} , preserving the triangular subdivision of \mathcal{F} , so that each sub-face satisfies $f^n = \Psi_{n,n+1}(f^{n+1})$. Then, the swept amount $\Delta U_{i,j,k,\mathcal{F}}^{n,n+1}$ is given by

$$\Delta U_{i,j,k,\mathcal{F}}^{n,n+1} = \frac{1}{V_{i,j,k}} \sum_{\{f^{n+1} \in \mathcal{F}^{n+1} \mid f^{n+1} \subset C_{i,j,k}\}} \sum_{\{C_{p,q,r} \mid K_f \cap C_{p,q,r} \neq \emptyset\}} \mathcal{V}_{p,q,r} U_{p,q,r}^n, \quad (14)$$

where $\mathcal{V}_{p,q,r}$ is the signed volume of the intersection between the prism K_f (whose bases are f^n and f^{n+1}) and the fluid grid cell $C_{p,q,r}$. The detailed procedure to compute the above quantities is described in [29], see also [24].

The fluid force acting on the solid particle I is given by

$$\vec{F}_{I,\text{fluid}}^n = \sum_{\mathcal{F} \in \mathfrak{F}_I} \vec{F}_{\mathcal{F},\text{fluid}}^n = - \sum_{\mathcal{F} \in \mathfrak{F}_I} \vec{\Pi}_{\mathcal{F}}^n, \quad (15)$$

where \mathfrak{F}_I collects the wet faces of the particle I . Similarly, the fluid torque $\vec{\mathcal{M}}_{I,\text{fluid}}^n$ is given by

$$\vec{\mathcal{M}}_{I,\text{fluid}}^n = \sum_{\mathcal{F} \in \mathfrak{F}_I} \vec{F}_{\mathcal{F},\text{fluid}}^n \wedge (\vec{X}_{\mathcal{F}}^n - \vec{X}_I^n). \quad (16)$$

The general procedure for the conservative coupling method can be described by the following steps:

- The fluid fluxes used in (6) are precomputed at all the cell faces of the fluid grid, without taking into account the presence of the solid.
- The solid internal forces and torques are computed based on the position of the solid particles.
- The fluid pressure forces and torques exerted on the solid are evaluated using (15) and (16).
- The solid is advanced in time.
- The volume fractions and side area fractions are computed using the new position of the fluid-solid interface. The fluid fluxes in (6) are modified using these volume fractions and side area fractions. At this stage, the swept amount is also calculated using (14).
- The solid flux is computed using (13), and the final value of the fluid state is calculated using (5).
- The small cut-cells are mixed and the solid cells are filled in order to prepare for the next time-step.

The fluid and the solid should advance with the same time-step. Thus, we use in the fluid and in the solid solvers the minimum between the fluid and the solid time-steps provided by the respective CFL stability conditions. The general structure of the time-explicit coupling scheme is summarized in Fig. 3.

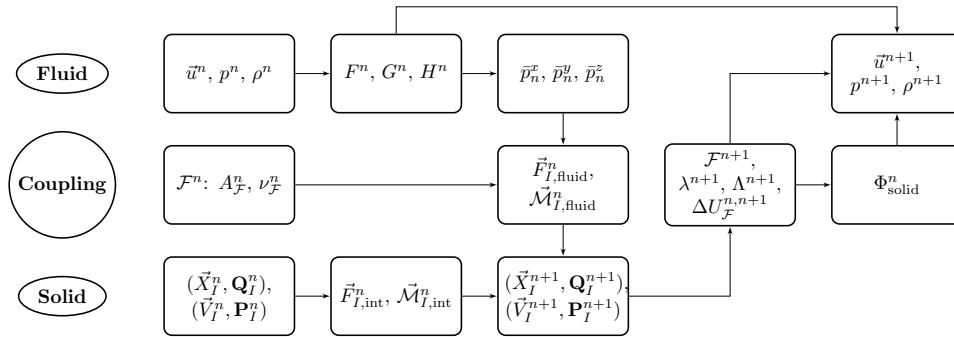


Figure 3: Time-explicit coupling scheme

3 Coupling with fragmenting structure

3.1 Solid fragmentation in the Discrete Element method

The Discrete Element method deals with solid fragmentation by breaking the link between particles (Fig. 4). The fracture propagates element by element using a fracture criterion defined at the contact faces between particles. Dynamic fragmentation using the Discrete Element method has been studied in [23], using both the discrete Camacho–Ortiz criterion [1] and the continuous Denoual et al. criterion [7]. The Camacho–Ortiz criterion expresses damage as a function of crack opening. When the local stress reaches a threshold, it decreases linearly with the crack opening until the fracture is open. The Denoual et al. criterion is a probabilistic criterion where the damage is introduced per unit volume using a Weibull probability distribution. The coupling method is independent of the breaking criterion used in the solid solver in order to break the link between particles. In the present work, we focus on the feasibility study of the coupling method to deal with fragmentation and we choose a simple breaking criterion, namely the elongation at break of the structure, which measures the ability of the material to elongate before rupture under load. The interaction behaviour law between the particles in term of forces and torques is still taken here linear elastic in order to simplify the presentation and to verify the conservation of energy by the coupling system. More complex laws between particles can be used by integrating them in the expression of internal forces and torques between particles.

The elongation at break $A\%$ is a dimensionless quantity which is a characteristic of the material and which is determined by a tensile test. In the case of a brittle material, the rupture occurs at the end of the elastic domain. The fracture surface is generally perpendicular to the axis of traction. The elongation at break is very low, for instance, for a cast iron it is in the range (0.3, 0.8), so that a 1m long beam cracks before its elongation reaches 8 mm.

For two neighboring particles I and J , we compute the elongation at break as follows:

$$A\% = 100 \frac{\|\vec{X}_I^n - \vec{X}_J^n\| - \|\vec{X}_I^0 - \vec{X}_J^0\|}{\|\vec{X}_I^0 - \vec{X}_J^0\|}.$$

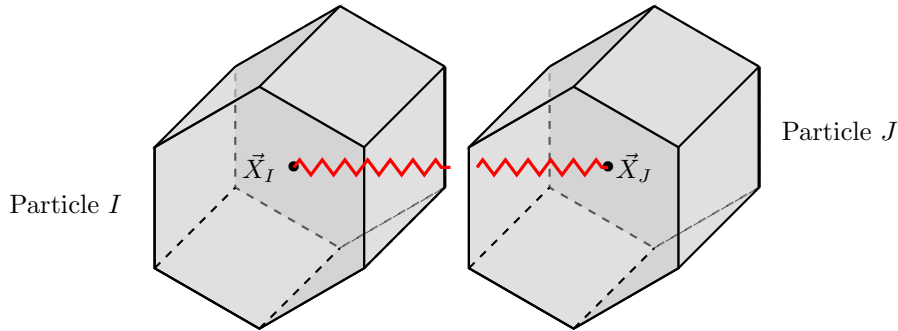


Figure 4: Broken link between particles

The swept amount and the boundary reconstruction are computed for every solid face, including the internal faces for which this treatment is not necessary (since contributions from solid vis-a-vis faces cancel). This allows for an effective management of new wet faces when fracture occurs as all faces follow the same treatment. An alternative approach could be to perform these treatments only for the internal faces for which there is a potential risk of fracture (when the elongation at break is close to a critical level).

3.2 Vacuum cells

During the process of fragmentation, vacuum between solid particles can occur due to the fact that the velocity of the crack propagation can be larger than the speed of sound in the fluid. For instance, in the case of the Griffith fracture model [16] for a linear elastic material, a theoretical analysis shows that the limiting fracture speed for mode I fracture is the Rayleigh wave speed, which can be estimated by

the following expression [10]:

$$c_R = c_s \frac{0.862 + 1.14\nu}{1 + \nu},$$

where ν is the Poisson ratio. The compression wave speed c_p (a wave in which the disturbance is a compression of the medium) and the shear wave speed c_s (a wave in which the disturbance is an elastic deformation perpendicular to the direction of motion of the wave) are given by following formulas:

$$c_p = \sqrt{\frac{E(1 - \nu)}{\rho(1 + \nu)(1 - 2\nu)}}, \quad c_s = \sqrt{\frac{E}{2\rho(1 + \nu)}},$$

where E is the Young modulus. For mode II and mode III, limiting speeds are the compression and shear wave speed, respectively [10].

The vacuum presence leads to fluid cells where the fluid pressure and the density are close to zero. Vacuum also occurs in the case of an internal fracture in the solid with no outlet in the fluid domain. In these cases, the solid cells ($\Lambda = 1$) can become cut cells or fluid cells ($0 \leq \Lambda < 1$) because there is a gap between particles, and the fluid occupying this gap has a very low pressure and density. This leads us to consider a new type of cell, the ‘‘vacuum cell’’, which is characterised by $\Lambda \leq 1$ and a fluid state with vanishing density and pressure.

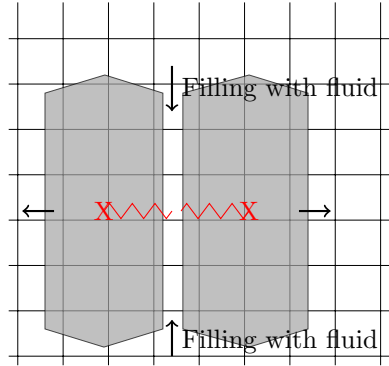


Figure 5: Fluid penetration into the crack due to the broken link between two solid particles

3.3 Riemann problem in the presence of vacuum

Once the link between particles is broken, the fluid should penetrate between these particles if there is a path between the fluid and the solid crack. Therefore, we have to compute the solution of the Euler equations in domains adjacent to regions of vacuum in order to fill the space between particles with fluid.

Let us consider the one-dimensional case of a fluid occupying the region $x < 0$ and a vacuum region in $x > 0$. This leads to the following Riemann problem:

$$U(x, 0) = \begin{cases} U_{\text{fluid}}, & \text{if } x < 0, \\ U_{\text{vacuum}}, & \text{if } x > 0, \end{cases}$$

where U_{fluid} and U_{vacuum} are the states in the fluid and vacuum regions, respectively. As in [35], we consider that $U_{\text{vacuum}} = (0, u_0, 0)$, where u_0 is the velocity of the interface between the two regions (due to the gradient of pressure) given by $u_0 = u_{\text{fluid}} + \frac{2c_{\text{fluid}}}{\gamma - 1}$, where c_{fluid} is the speed of sound in the fluid such that $c_{\text{fluid}}^2 = \frac{\gamma p_{\text{fluid}}}{\rho_{\text{fluid}}}$, where u_{fluid} , ρ_{fluid} , and p_{fluid} are the velocity, mass density, and pressure in the fluid region. The analytical solution of this Riemann problem can be found in [35]. Herein, we treat the interface between a vacuum cell and a fluid cell by solving the same Riemann problem, U_{fluid} being the state of the fluid cell in contact with vacuum. This Riemann problem is solved numerically using the Lax–Friedrichs flux, given by

$$F_{i+1/2,j,k}^n = \frac{1}{2} (F_{i,j,k}^n + F_{i+1,j,k}^n) - \frac{\Delta x_{i,j,k}}{2\Delta t} (U_{i+1,j,k}^n - U_{i,j,k}^n).$$

We have chosen this flux because it does not involve any division by pressure or density. It is known that this flux is dissipative [21]. The use of the Lax–Friedrichs flux is limited around the crack region. Once a vacuum cell is filled with fluid, it is no longer a vacuum cell, and the usual OSPM flux is used in the subsequent time-steps.

3.4 Mixing of small cut-cells

Several solid boundaries may be present in a cut cell after the fragmentation of the solid. Let us consider the situation illustrated in Fig. 5. Two vis-à-vis solid particles are present in one small cut-cell. In the direction of the outward normal to the solid boundary the cells are entirely occupied by the solid, and the neighboring cells are also small cut-cells. Therefore, the usual mixing of small cut-cells cannot be employed. To deal with this situation, we look for a target cell using a recursive algorithm. If the neighboring cells are all either solid cells or small cut-cells, we choose the neighboring cut cell with the largest face aperture as temporary target cell. We iterate until we find a fluid cell or come into a cycle (in this case the target cell is the last cell found before cycling). This ensures that there exists a target cell as well as a fluid path from the original small cut-cell to the target cell.

Let C_{target} be a fluid cell that has been found as a target cell and U_{target} the fluid state in that cell. Let $\mathcal{C}_{i,j,k}$ collect all the small cut-cells having C_{target} as target cell. Defining

$$U_{\text{Mix}} = U_{\text{target}} + \sum_{C_{i,j,k} \in \mathcal{C}_{i,j,k}} (1 - \Lambda_{i,j,k}) U_{i,j,k}, \quad \text{and} \quad V_{\text{Mix}} = 1 + \sum_{C_{i,j,k} \in \mathcal{C}_{i,j,k}} (1 - \Lambda_{i,j,k}),$$

then the new state in C_{target} is $U_{\text{target}} = \frac{U_{\text{Mix}}}{V_{\text{Mix}}}$. The new state for all $C_{i,j,k} \in \mathcal{C}_{i,j,k}$ is U_{target} .

The mixing procedure is conservative and ensures that the equivalent volume of a small cut-cell is compatible with the CFL condition (2) using the standard-size cells.

4 Numerical results

In this section, we present numerical results. We first verify the conservation properties of the scheme and the propagation of the fluid in opening fractures in a three-dimensional structure. Then, we simulate the effect of an internal explosion in a steel cylinder in two space dimensions. Finally, we consider an overpressure inside a cube with mobile walls.

4.1 Flow through opening fractures in 3d

In this test case, we consider a three-dimensional structure composed of two particles and immersed in a fluid at rest. We assume that one particle is fixed, and that the other is displaced with a prescribed velocity, leading to an opening fracture between the two particles. As the opening velocity is high, a vacuum region is created between the two particles and is progressively filled with fluid. The fluid domain is the box $[0, 2] \times [0, 2] \times [0, 2]$ m. The initial fluid state is given by $(\rho, \vec{u}, p) = (1.4\text{kg}\cdot\text{m}^{-3}, \vec{0}\text{m}\cdot\text{s}^{-1}, 1\text{Pa})$. The computation is carried out until $t = 0.25\text{s}$. Three uniform grids are considered for the fluid with reflecting boundary conditions. The first grid contains $(75 \times 75 \times 75)$ cells, the second $(100 \times 100 \times 100)$ cells, and the third grid $(125 \times 125 \times 125)$ cells. The computation is carried out until $t = 0.25\text{s}$. The solid is discretized with two parallelepipedic particles, having the same dimensions $(0.4, 0.8, 0.8)$ m and their centres of mass are located at $(0.8, 1, 1)$ m and $(1.2, 1, 1)$ m. The first particle, i.e. the left particle, is motionless, and the second particle, i.e. the right particle, has a prescribed velocity $\vec{V} = 1\vec{e}_x\text{m}\cdot\text{s}^{-1}$.

Kinetic energy is transferred from the mobile particle to the fluid, and the particle displacement generates a compression wave in the fluid at the right of the moving particle, and a rarefaction wave propagates inside the opening fracture. In Fig. 6, we display 30 density iso-contours in the plane $\{z = 1\}$ m at times 0.07s, 0.1s, 0.15s, and 0.25s using grid 3. At time $t = 0.07\text{s}$, the gap is filled with fluid having low density compared to the density of the external fluid. At later times, the density between the two particles increases, and shock waves propagate over the fluid domain.

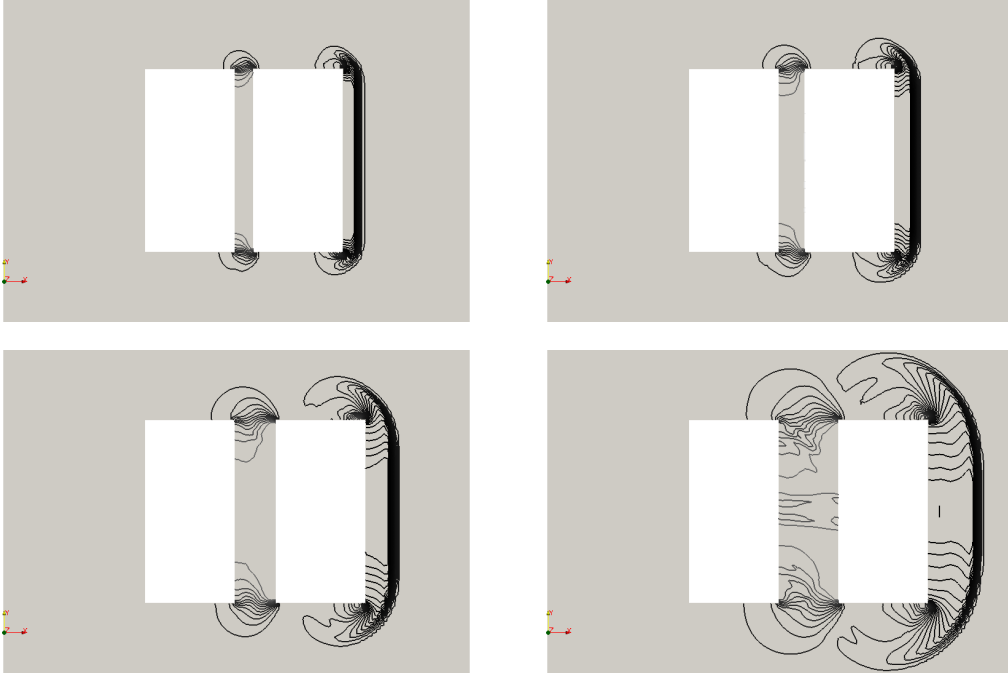


Figure 6: 30 density iso-contours in the plane $\{z = 1\}$ m on grid 3 at times 0.07s, 0.1s, 0.15s, and 0.25s from left to right and top to bottom.

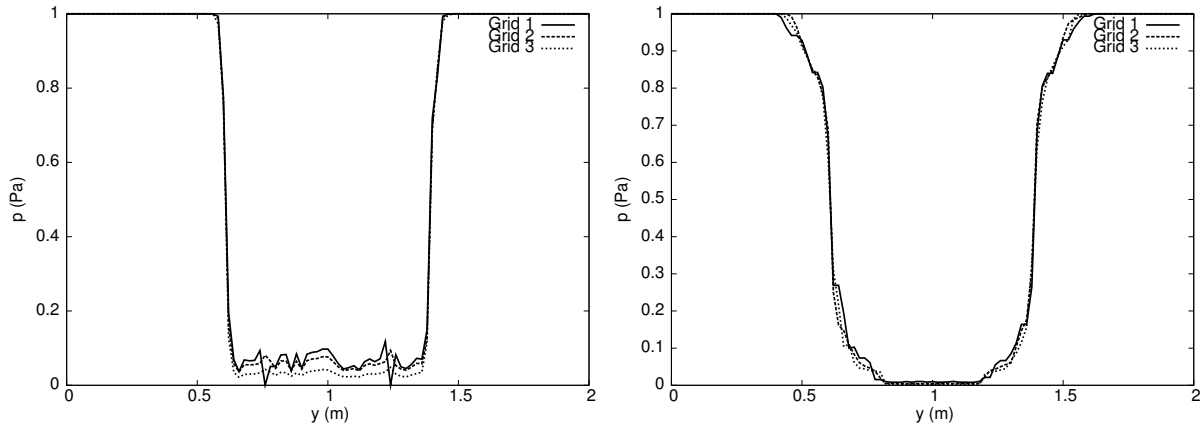


Figure 7: Pressure distribution along the line $\{x = 1, z = 1\}$ m on grid 1, grid 2, and grid 3 at times 0.01s (left) and 0.12s (right).

The pressure distribution along the line $\{x = 1, z = 1\}$ m (this line passes through the middle of the opening fracture) on grids 1, 2, and 3 is shown in Fig. 7 at times 0.01s and 0.12s. At time $t = 0.01$ s for the three grids the opening fracture is filled with fluid. The opening fracture is very small, and the fluid cells inside the fracture are small cut-cells. The pressure variations are related to the mixing procedure applied to these small cut-cells. At time $t = 0.12$ s, as the solid has continued to pull the fluid as a piston, the pressure is very low in the center of the opening fracture. The situation at the edges of the opening fracture resembles that of a shock tube: rarefaction waves are generated in the fluid near the opening edge, while compression waves in the fracture tend to increase the pressure inside the fracture. We notice that the pressure inside the opening fracture is fairly well-converged, although the profiles remain slightly grid-dependent. The pressure difference is due to the fact that there is less numerical diffusion when the mesh is refined. The vacuum cells represent 0.2% of the total grid cells for grid 1, 0.15% for grid 2, and 0.12% for grid 3 at the opening time and progressively disappear.

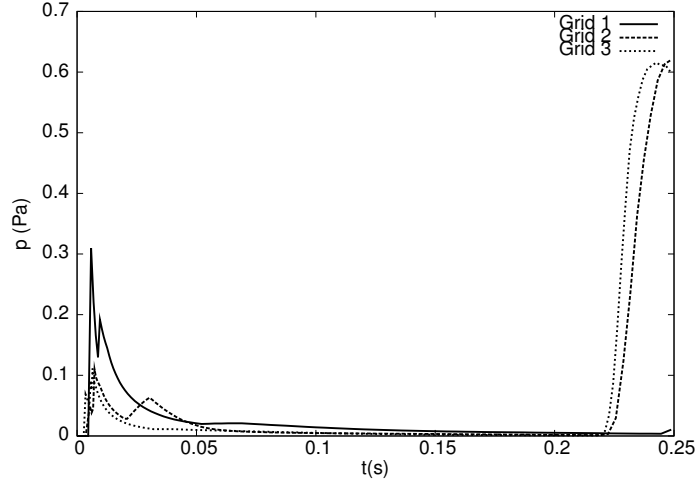


Figure 8: Time evolution of the pressure in the center of the opening fracture for three fluid grids.

Fig. 8 illustrates the time evolution of the pressure at the point $(1, 1, 1)m$ situated at the center of the opening fracture for the three fluid grids. We observe that the first peak of pressure decreases with mesh refinement. We attribute the existence of these peaks to the mixing procedure, that is grid dependent, once the vacuum cells are filled with fluid. After the time $t = 0.23s$, the pressure increases due to the compression waves that reach the face of the mobile particle (except for grid 1, in which the grid is not fine enough to fully capture these waves).

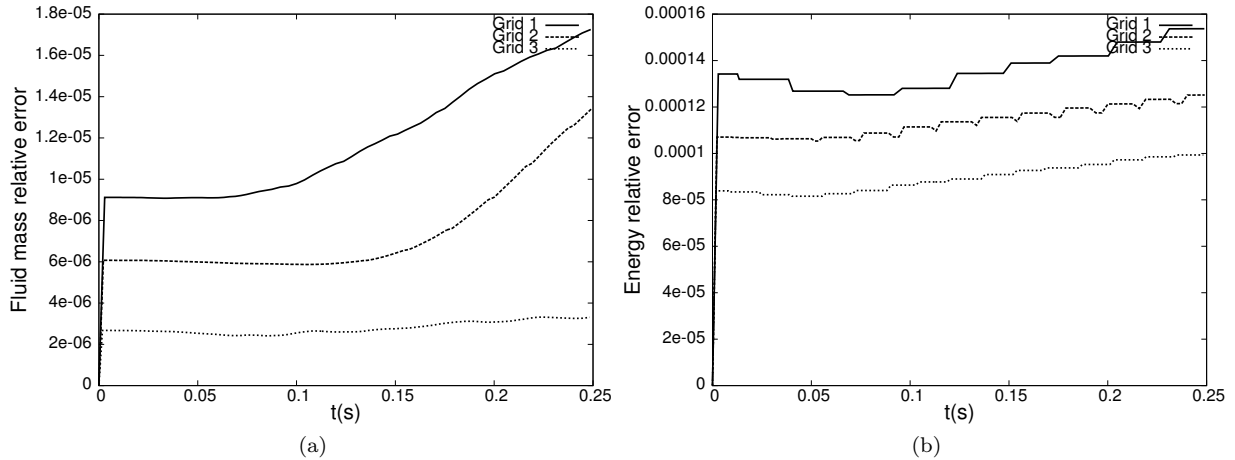


Figure 9: Relative conservation error on (a) fluid mass and (b) system energy for three fluid grids.

In Fig. 9a we present the relative conservation error of fluid mass, computed as the difference between the initial mass and the mass at the different time-steps for the three fluid grids. The mass difference is normalized by the maximum amount of mass swept by the movement of the solid. In Fig. 9b we present the relative energy conservation error, computed as the difference between the initial energy and the energy at the different time-steps for the three grids. This energy difference is normalized by the maximum energy exchange between the fluid and the solid. We observe that the relative conservation error on mass and energy is extremely low and decreases with grid refinement. In fact, these errors are at the same level as in the case of a rigid solid [29]. For instance, the relative mass error is as low as 0.003%, and the relative energy error is as low as 0.01% for grid 3. The main effect accounting for mass and energy variations are the round-off errors involved in the evaluation of geometric quantities in cut cells. The variation of the energy is larger than the variation of the mass. This originates from the time-integration scheme for the solid which does not ensure the conservation of the exact discrete energy. Like many symplectic schemes, the scheme preserves an approximate discrete energy over long-

time simulations. This typically induces fluctuations of the exact discrete energy of the solid around a mean value [25]. Interactions between these fluctuations and the conservative fluid occur. However, the overall conservation of energy for the system is very good.

4.2 Internal explosion in a steel cylinder in 2d

In this test case, we simulate an internal explosion in a shell formed by a steel cylinder in two space dimensions. The cylinder is initially surrounded by gas at atmospheric pressure, and contains gas at the same pressure. An overpressure region is initiated inside the cylinder resulting in shock waves impinging the inner cylinder wall. The computational domain is the rectangle $[0, 30] \times [0, 15]$ m. The computation is performed on a 600×300 fluid grid. The boundaries of the domain are reflecting boundaries. The cylinder is centered at $(15, 7.5)$ m with a thickness of 0.2m and an interior radius of 5m. The cylinder is discretized with 50, 100, and 200 particles along its circumference and 1 particle in thickness. Initially, the state of the gas is

$$\begin{cases} \rho = 99.935\text{kg.m}^{-3}, \vec{u} = \vec{0}\text{m.s}^{-1}, p = 50,662,500\text{Pa} & \text{if } (x, y) \in D((13, 7.5)\text{m}, 1\text{m}), \\ \rho = 0.118\text{kg.m}^{-3}, \vec{u} = \vec{0}\text{m.s}^{-1}, p = 10,132.5\text{Pa} & \text{otherwise,} \end{cases}$$

where $D((x_0, y_0), R)$ denotes the disk centred at (x_0, y_0) with radius R . In Fig. 10, we display the initial density field of the fluid and the initial position of the cylinder. The density and the Young modulus of the cylinder are, respectively, $\rho_s = 7860\text{kg.m}^{-3}$ and $E = 210\text{GPa}$, with a Poisson ratio $\nu = 0$. In this test case, the elongation at rupture is set at 1%. The simulation time is $t = 0.0244\text{s}$.

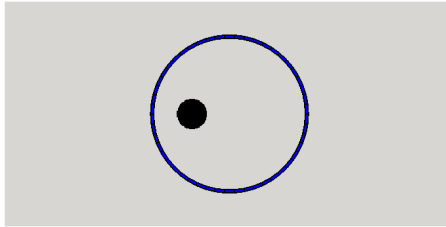


Figure 10: Density profile in the fluid and cylinder position at time $t = 0\text{s}$.

After impacting the inner cylinder wall, the shock wave partially reflects, while part of its energy is transferred as kinetic energy to the cylinder. At the same time, the cylinder is deformed, and pressure waves travel along its surface. In Fig. 11, we show the density field in the fluid and the normal stress distribution in the cylinder at times 2.5ms, 5ms, 7ms, 13ms, 20ms, and 24.4ms when the cylinder is discretized with 50 particles. In Fig. 12, we show the density field in the fluid and the normal stress distribution in the cylinder at time 24.4ms when the cylinder is discretized with 100 and 200 particles. We notice that, in all three cases the rupture takes place at the left and right side of the cylinder, in approximately the same areas. Convergence of brittle fractures requires a large number of particles [23]. As the solid particles must have a thickness larger than or equal to two fluid grid cells, it would be necessary to use an adaptive meshing refinement in order to study the convergence of brittle fractures. We also notice that the fluid behavior is very similar inside the cylinder independently from the solid discretization. The main difference occurs in the regions where fluid flows through the cracks. The difference in crack patterns mainly changes the contact discontinuity pattern in the fluid outside the cylinder. The shock waves are reflected inside the cylinder and weak compression waves are transmitted by the movement of the solid outside the cylinder near the impacted regions of the cylinder. Several links between particles are broken, and the pressure waves in the solid propagate only in a few particles. We remark that the fluid penetrates into the opening gap between the particles and that the shock waves also propagate outside the cylinder. In Fig. 13, we illustrate the time evolution of the fluid pressure in the cell containing the point $(10, 7.5)$ m situated near the particle closest to the explosion inside the cylinder

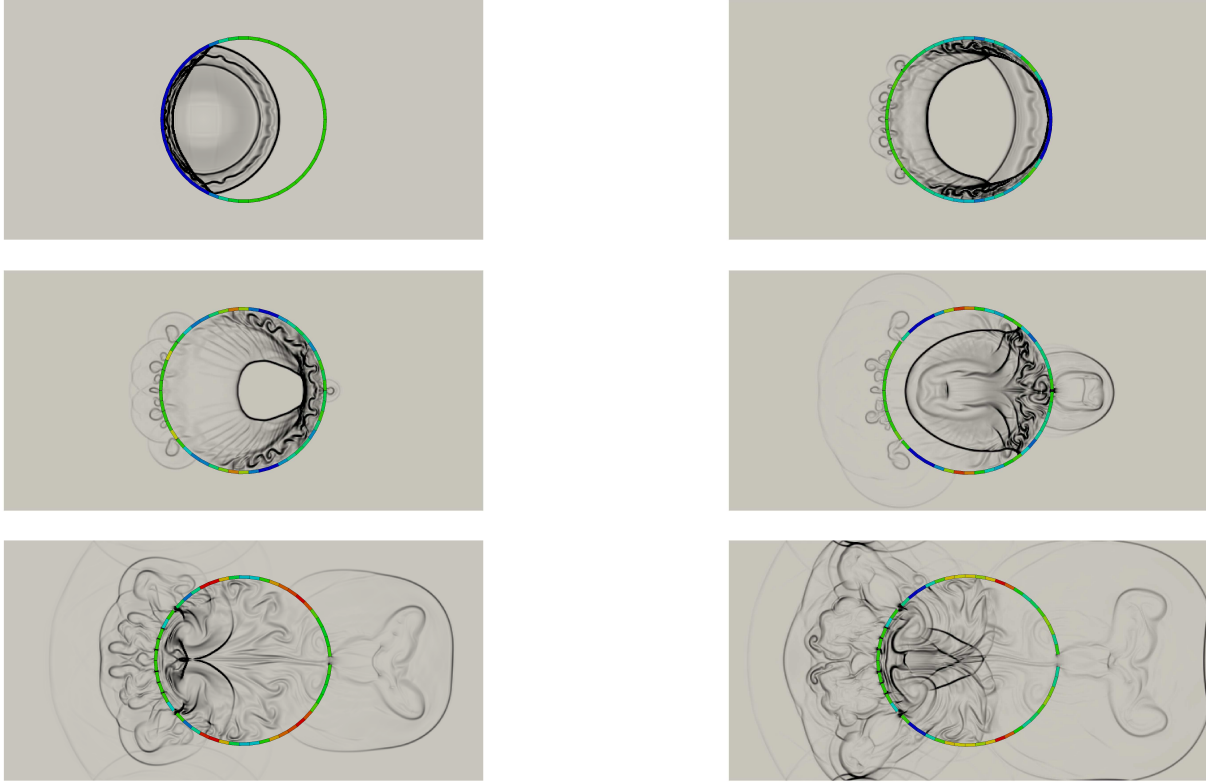


Figure 11: Density field in the fluid and normal stress distribution in the cylinder discretized with 50 particles at times 2.5ms, 5ms, 7ms, 13ms, 20ms, and 24.4ms from left to right and from top to bottom.

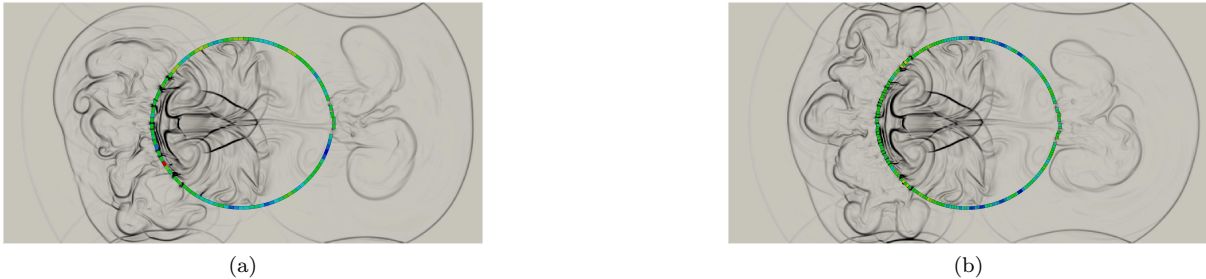


Figure 12: Density field in the fluid and normal stress distribution in the cylinder discretized with (a) 100 particles and (b) 200 particles at time 24.4ms.

and in the cell containing the center of the domain $(15, 7.5)m$ for the three cylinder discretizations. In Fig. 13a, we notice that the pressure increases as the shock wave reaches the point, and then decreases as the shock wave is reflected by the solid boundary near this point. Peaks observed later on are due to reflected shock waves reaching the point after several other reflections on different points of the inner solid boundary. In Fig. 13b, the first peak corresponds to the shock wave passing through the point. The second one corresponds to reflected shock waves that reach the point after several reflections on the inner solid boundary. This second peak is stronger than the first one due to the refocusing of shock waves inside the cylinder. We notice that the pressure patterns are remarkably similar independently from the solid discretization.

Complex interaction between the waves travelling on the surface of the cylinder and the fluid occur, accounting for successive compression and traction phenomena in the cylinder leading to fractures located in the closest and farthest regions to the explosion. In Fig. 14, we display the time evolution of the normal stress in the solid particle closest to the explosion (centred initially at $(9.91006, 7.82023)m$) and in the

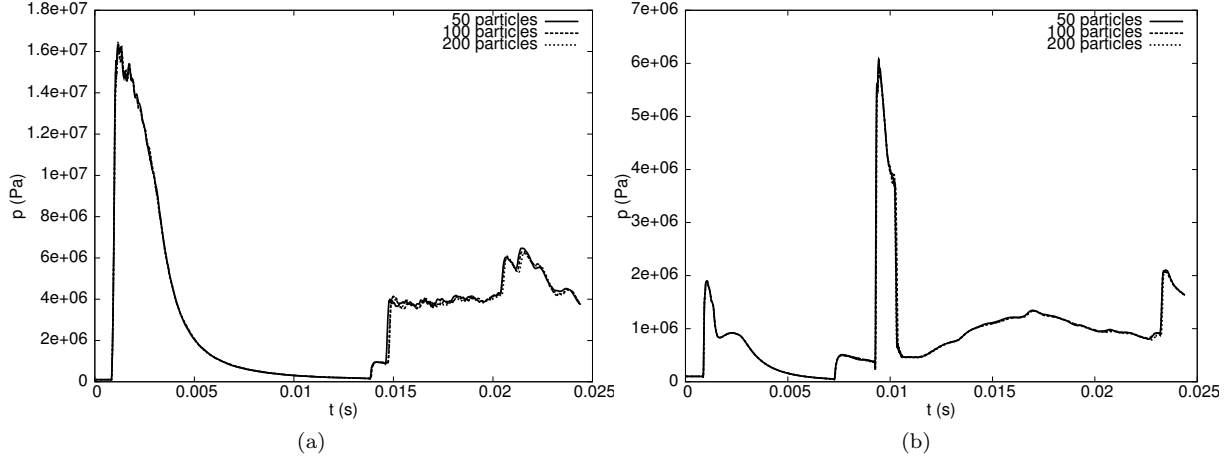


Figure 13: Time evolution of the fluid pressure in the cell containing (a) the point (10, 7.5)m situated near the particle closest to the explosion inside the cylinder and (b) the point (15, 7.5)m located at the center of the domain for the three cylinder discretizations.

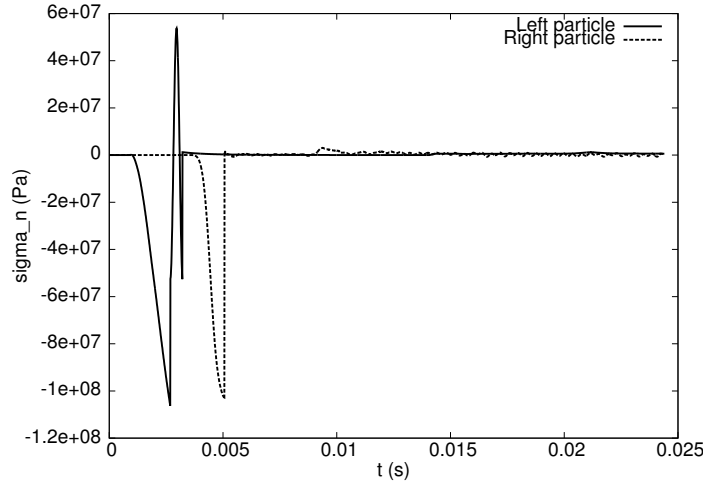


Figure 14: Evolution of the normal stress in the solid particle closest to the explosion (left particle) and in the solid particle farthest to the explosion (right particle) when the cylinder is discretized with 50 particles.

solid particle farthest to the explosion (centred initially at (20.0899, 7.82023)m) when the cylinder is discretized with 50 particles. For the particle closest to the explosion, we notice that the normal stress decreases up to the time $t = 2.6$ ms, where the link with one neighbor is broken. Immediately after this moment, the normal stress increases up to the time $t = 3.2$ ms when the link with the other neighbor is broken. As the particle has no link with other particles, the normal stress gets back to zero. For the particle farthest to the explosion, the normal stress decreases and reaches its minimum value at time $t = 5$ ms, where the link with one neighbor is broken. After that, the normal stress oscillates with a smaller amplitude. The link with the other neighbor is not broken as the normal stress does not reach a high enough value. The particles are enumerated counter-clockwise, the first particle being centred initially at (20.0899, 7.82023)m when the cylinder is discretized with 50 particles. In Tab. 1, we report for each broken link the number of the two involved particles and the time when the link is broken when the cylinder is discretized with 50 particles. For the particles closer to the explosion, the links are broken when the shock waves impact that region. For the particle farthest to the explosion, the links are broken when the waves travelling on the surface of the cylinder meet. In Fig. 15, we show the relative displacement between each particle and its counter-clockwise neighbor at times 7ms, 13ms, 20ms, and 24.4ms when the cylinder is discretized with 50 particles. We observe that the relative displacement between linked

Particles	Time (ms)
23 - 24	2.6
25 - 26	
27 - 28	
20 - 21	2.8
30 - 31	
24 - 25	3.2
26 - 27	
22 - 23	3.5
28 - 29	
1 - 50	5

Table 1: Broken links summary.

particles remains almost zero, whereas it is not the case for the particles with broken links. In Fig. 16, we show the relative displacement between each particle and its counter-clockwise neighbor at time 24.4ms when the cylinder is discretized with 100 and 200 particles. Fracture is a threshold phenomenon, thus the symmetry is not exact. The more particles we have, the more breaking links occur. We notice that fragments are similarly located in all three cases with more fragments on the left side compared to the right side.

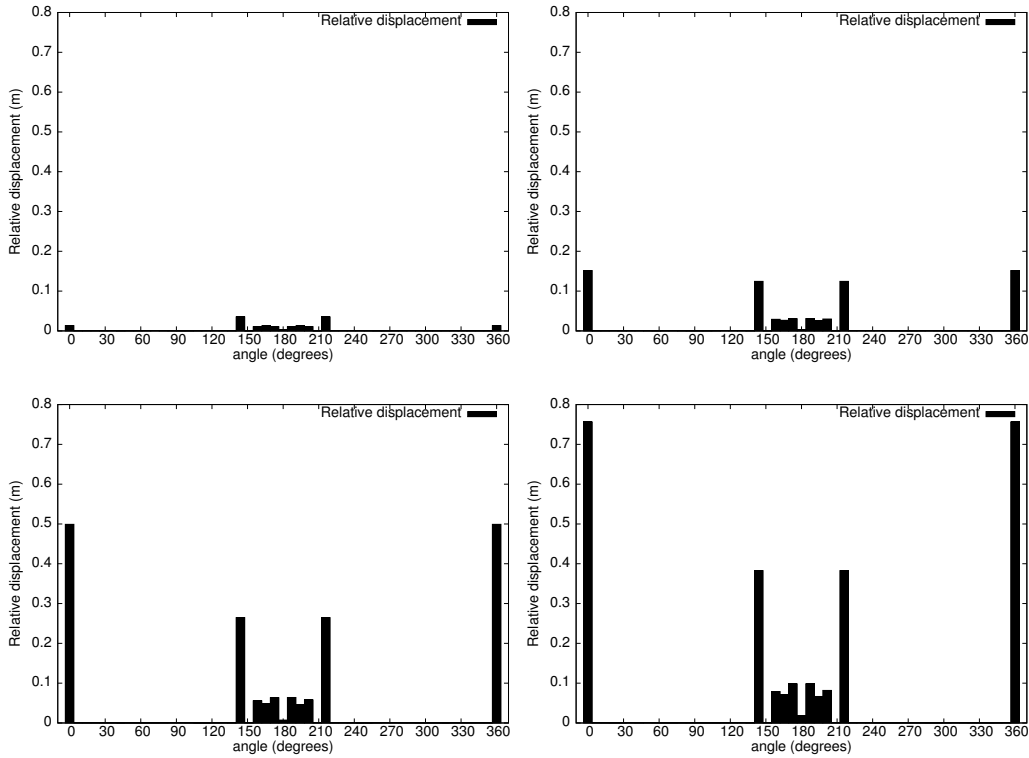


Figure 15: Relative displacement between each particle and its counter-clockwise neighbor at times 7ms, 13ms, 20ms, and 24.4ms from left to right and from top to bottom when the cylinder is discretized with 50 particles.

In Fig. 17, we display the displacement as a function of time of the center of mass of the solid particle closest to the explosion and that of the solid particle farthest to the explosion when the cylinder is discretized with 50 particles. We notice that the closest particle begins its movement along the x -axis around the time $t = 2$ ms, while the farthest particle begins its movement along the same axis later on, at time $t = 7$ ms. In both cases, the times correspond to a shock wave reaching the particle. The displacement of the closest particle has larger amplitude along the x -axis. The overpressure is higher near

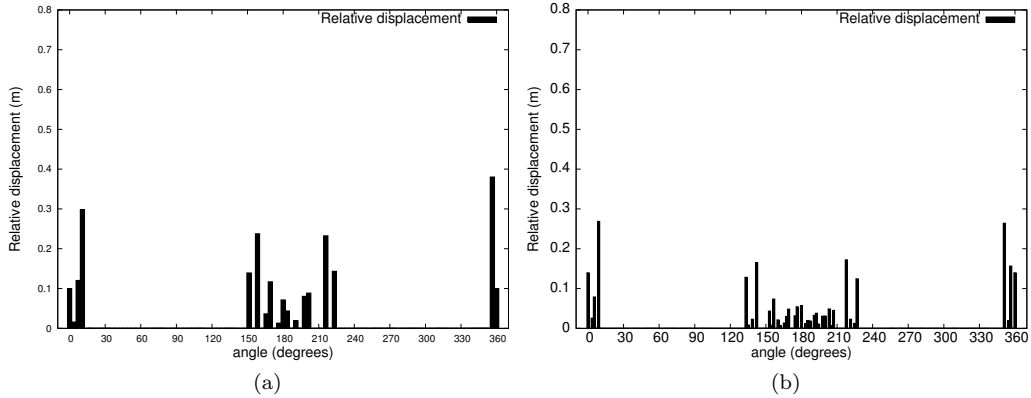


Figure 16: Relative displacement between each particle and its counter-clockwise neighbor at time 24.4ms when the cylinder is discretized with (a) 100 particles and (b) 200 particles.

this particle, which broke the link with both of its neighbors, followed by a ballistic flight. Concerning the displacement along the y -axis, the closest particle exhibits very little displacement compared to the farthest particle. The farthest particle is still attached to other particles and is subjected to flexion moments from the rest of the solid.

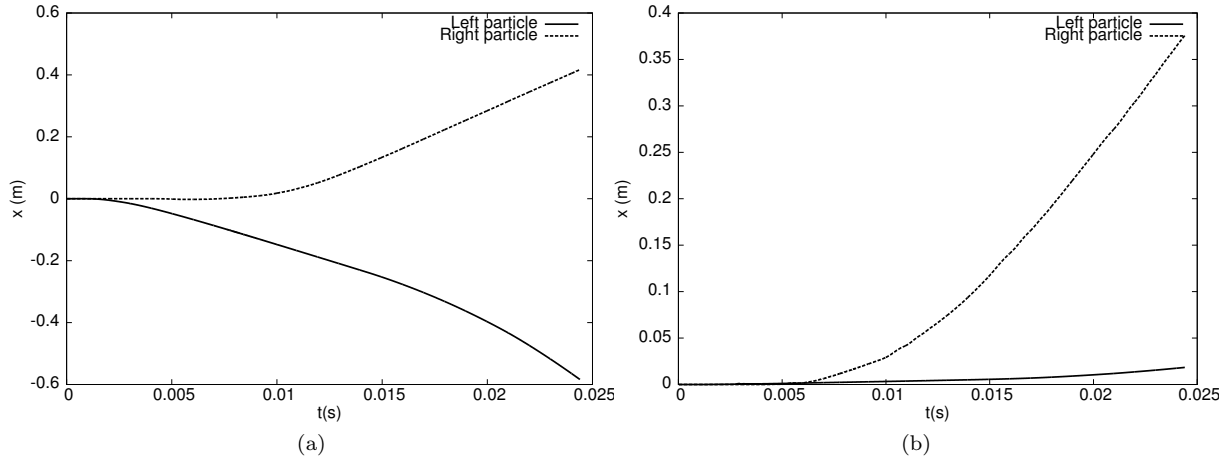


Figure 17: (a) x -coordinate and (b) y -coordinate of the center of mass of the solid particle closest to the explosion (left particle) and of the solid particle farthest to the explosion (right particle) as a function of time when the cylinder is discretized with 50 particles.

In Fig. 18, we show the time evolution of the kinetic solid energy and the dissipated energy when the cylinder is discretized with 50 particles. The dissipated energy exhibits jumps whose amplitudes correspond to energy lost by breaking links between particles. In Fig. 19a, we present the relative conservation error of fluid mass (computed as before) for the three cylinder discretizations. As before, the main effect accounting for this variation are the round-off errors involved in the evaluation of geometric quantities in cut cells. The variation of mass is as low as $6 \cdot 10^{-7}\%$ of the mass swept by the solid. In Fig. 19b, we present the relative energy conservation error, computed as the difference between the initial energy, the dissipated energy, and the energy at the different time-steps for the three cylinder discretizations. This energy difference is normalized by the maximum energy exchange between the fluid and the solid. We observe a variation of both mass and energy. As before, the main effect accounting for this variation are the round-off errors involved in the evaluation of geometric quantities in cut cells and the symplectic time-integration scheme for the solid. When links break, extremely rapid changes in internal forces between particles occur. As the fracture does not occur in exactly the same way for the three discretizations, the energy changes accordingly. The variation of energy is as low as 0.1% of the

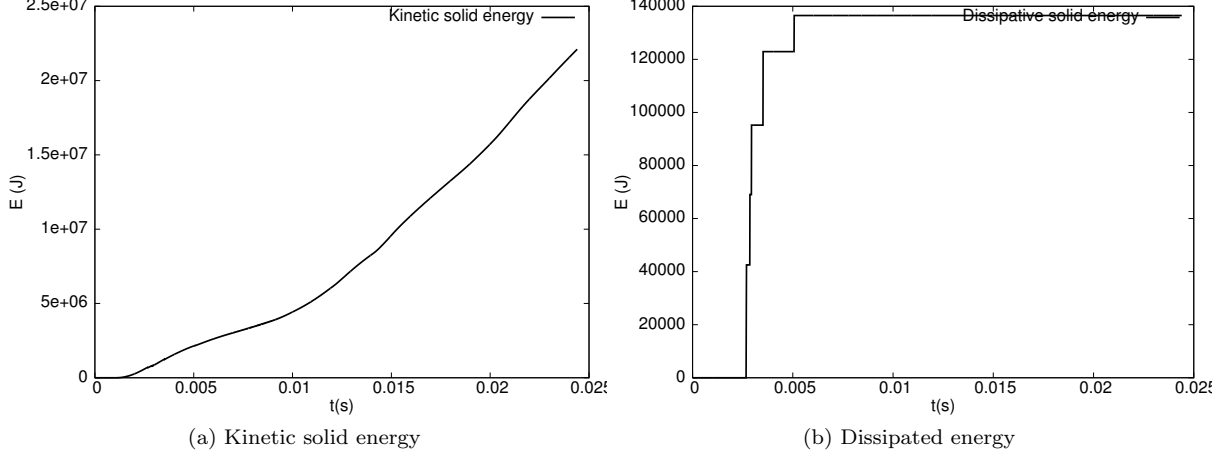


Figure 18: Time evolution of the kinetic solid energy and of the dissipated energy when the cylinder is discretized with 50 particles.

energy exchange in the system in all three cases, which is a very low level of error.

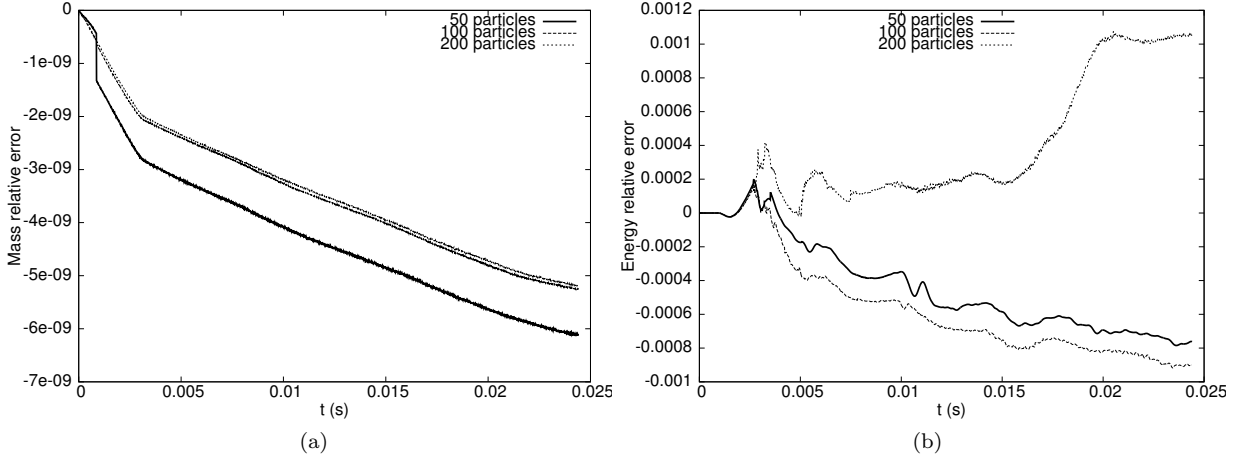


Figure 19: Relative conservation error on (a) fluid mass and (b) system energy for the three cylinder discretization.

4.3 Overpressure inside a cube with mobile walls

In this test case, an overpressure region is initiated inside a rigid cubic structure with mobile walls. In this test case, the rigid walls are not linked, but opening gaps appear between the solid walls as they are pushed away from each other by the shock wave produced by the overpressure. The fluid domain is the box $[0, 2] \times [0, 2] \times [0, 2]$ m, and the initial fluid state is given by

$$\begin{cases} \rho = 8. \text{ kg.m}^{-3}, \vec{u} = \vec{0} \text{ m.s}^{-1}, p = 116.5 \text{ Pa} & \text{if } (x, y) \in D((1.1, 1., 1.), 0.1) \text{ m,} \\ \rho = 1.4 \text{ kg.m}^{-3}, \vec{u} = \vec{0} \text{ m.s}^{-1}, p = 1 \text{ Pa} & \text{otherwise,} \end{cases}$$

where $D((x_0, y_0, z_0), R)$ denotes the sphere centred at (x_0, y_0, z_0) with radius R . The simulation time is $t = 1$ s. The computation is performed on a $(100 \times 100 \times 100)$ fluid grid with periodic boundary conditions. The solid is composed of six particles. Each particle is a parallelepiped representing a mobile wall of the rigid cubic structure. The particles are described in Tab. 2. For each particle, we indicate the initial position of its center of mass (Center), and its dimensions $(\Delta x, \Delta y, \text{ and } \Delta z)$.

Particle	Center (m)	Δx	Δy	Δz
1	(0.65, 1, 1)	0.1	0.8	0.6
2	(1, 0.65, 1)	0.6	0.1	0.6
3	(1, 1, 0.65)	0.8	0.8	0.1
4	(1.35, 1, 1)	0.1	0.8	0.6
5	(1, 1.35, 1)	0.6	0.1	0.6
6	(1, 1, 1.35)	0.8	0.8	0.1

Table 2: Characteristics of the six particles forming the cubic structure.

The overpressure generates a shock wave impinging the solid. The shock wave propagates spherically and impacts first particle 4 as it is the closest to the overpressure zone. The shock wave is partially reflected, while part of its energy is transferred as kinetic energy to the particle. In Fig. 20, we display density iso-contours at times 0.07s, 0.1s, 0.14s, and 0.3s. The shock waves propagate inside the cubic structure, and reflect on particles leading to their displacements. We notice the displacement of particles due to energy transfer from the fluid. This leads to a gap between particles, so that the fluid can flow outside the cubic structure.

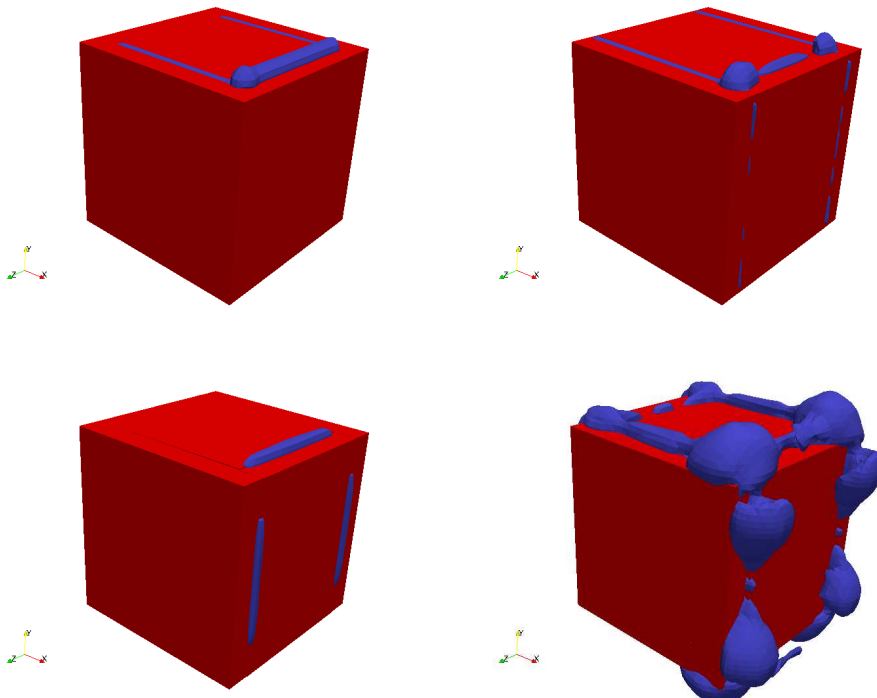


Figure 20: Density iso-contours at times 0.07s, 0.1s, 0.14s, and 0.3s from left to right and from top to bottom.

In Fig. 21, we display 30 density iso-contours in the plane ($z = 1$)m at times 0.07s, 0.1s, 0.14s, and 0.3s. We notice that as soon as the displacement of the particles leads to gaps, the fluid leaks outside the cubic structure. We also observe a few weak compression waves in the exterior fluid due to the movement of the particles. In Fig. 22, we show the displacement as a function of time of the center of mass of each particle. For particles 1 and 4, we display the x -coordinate of their center of mass because the displacements of these particles is along the x -axis due to the symmetry of the problem. Likewise, for particles 2 and 5, we display the y -coordinate of their center of mass, and for particles 3 and 6, we display the z -coordinate of their center of mass. The overpressure is almost at the center of the solid and the movement in the x , y , and z directions are of same order of magnitude for the particles which have the same mass. The movement of the particles is smooth despite successive impinging shock waves. This

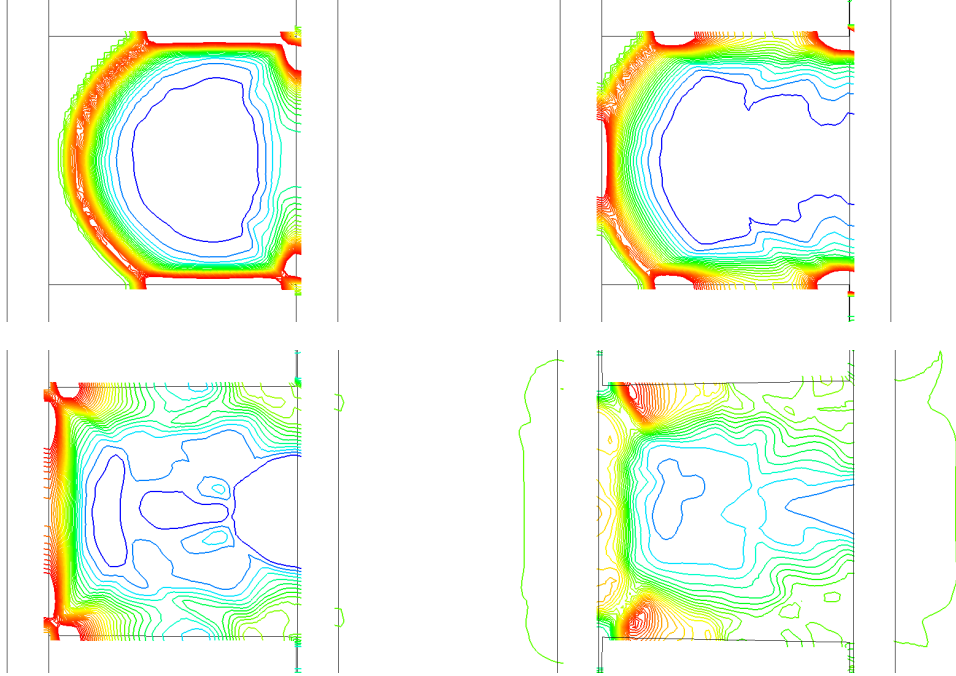


Figure 21: 30 density iso-contours in the plane ($z = 1$)m at times 0.07s, 0.1s, 0.14s, and 0.3s from left to right and from top to bottom.

is due to the effect of particles inertia. At the end of the simulation, the displacement of the particles is almost equal to half of the particles thickness.

The pressure distribution along the line $\{x = 1.3, z = 1\}$ m is shown in Fig. 23 at times 0.07s, 0.1s, 0.14s, 0.3s, 0.6s, and 0.9s. This line is close to the inner face of particle 4. The pressure varies along the y -axis. At time $t = 0.07$ s, the pressure is high at both y -extremities of particle 4. We observe in Fig. 22 that the displacement of particle 4 starts around this time. At time $t = 0.1$ s which corresponds to the beginning of the displacement of particles 3 and 6, pressure has soared on the extremities while it remains steady in the middle of the face of the particle. At time $t = 0.14$ s which corresponds to the beginning of the displacement of particle 1, pressure has decreased even in the middle of the line (underpressure), and we notice a small compression wave corresponding to the leaking of the fluid through the gap. At time $t = 0.3$ s, pressure has slightly increased along the line due to the arrival of the reflected waves on the solid face. The fluid continues to leak between the gaps, and at time $t = 0.6$ we observe that the corresponding compression waves increase since the pressure near particle 4 decreases. At time $t = 0.9$ s, the pressure is almost constant along the line.

Fig. 24a and Fig. 24b illustrate the time evolution of the pressure in the cell containing the points $(1.3, 1.4, 1)$ m and $(1.3, 0.6, 1)$ m respectively, which are situated at the outside corners of particle 4. We observe initially a small decrease of pressure due to the fact that the fluid is sucked into the gap, then an increase of pressure due to the overpressure leaking from the cube through the opening between particles. The two curves maintain good symmetry despite the coarseness of the mesh. Fig. 24c illustrates the time evolution of the pressure in the cell containing the point $(1.3, 1, 1)$ m which is located inside the cubic structure and near particle 4. We observe the initial overpressure, and then the effect of the reflection of the shock waves on particles.

Fig. 25 shows the evolution of the solid energy. Part of the shock waves energy is transferred to the particles as kinetic energy. This energy increases linearly to reach the value of 0.12J at time $t = 0.7$ s. In Fig. 26a, we present the relative conservation error of fluid mass (computed as before), and in Fig. 26b, we present the relative energy conservation error (computed as before). We observe a small variation of both mass and energy. As before, the main effect accounting for this variation are the round-off errors involved in the evaluation of geometric quantities in cut cells and the symplectic time-integration scheme for the solid. The variation of mass is as low as 0.003% of the mass swept by the solid. The variation of energy is as low as 0.03% of the energy exchange in the system.

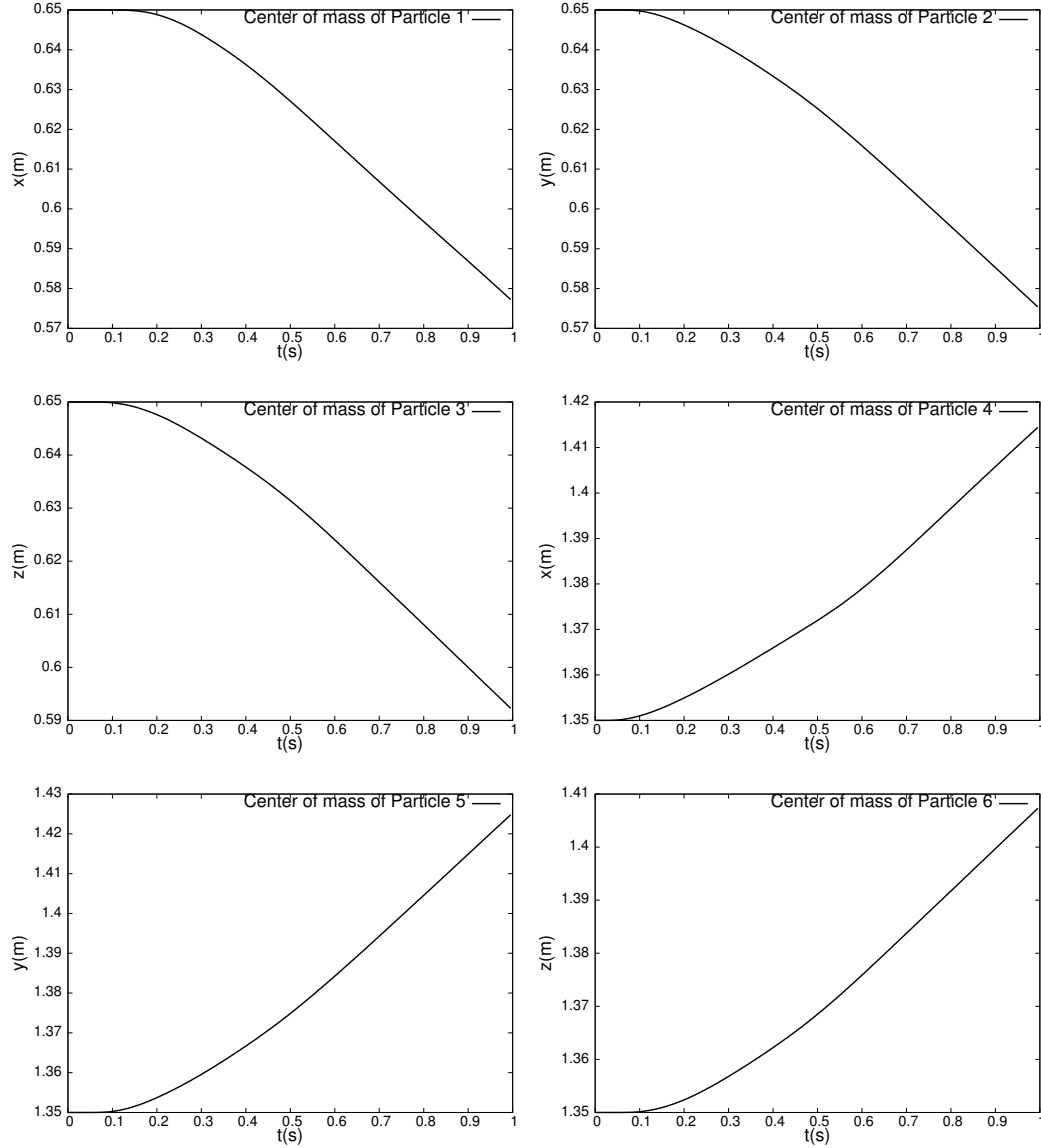


Figure 22: Position of the center of mass for the six particles.

5 Conclusion

In this work, we have developed a conservative method for the interaction between an inviscid compressible flow and a fragmenting structure. On the fluid side, we considered an inviscid Euler fluid in conservative form discretized by a Finite Volume method. On the solid side, we considered a fragmenting solid discretized by a Discrete Element method. An Immersed Boundary technique was employed through the modification of Finite Volume fluxes in the vicinity of the solid. During the process of fragmentation, vacuum between solid particles can occur, and the Lax–Friedrichs flux was employed to solve the corresponding Riemann problem. The coupling algorithm is based on an explicit time-marching procedure, it does not require remeshing of the fluid or solid domain, and allows fluid to pass through the fractured areas of the structure without any a priori knowledge of where fracture occurs.

The presented numerical simulations allowed us to illustrate the viability of the method in the case of two- and three-dimensional fragmenting solids coupled to an inviscid compressible flow with fluid flows through opening cracks. The prospect for continuing this work is to enrich the algorithm to take into account the possible contact between particles during the ballistic flight after fragmentation and to move on to more complex test cases. These developments are the subject of ongoing work.

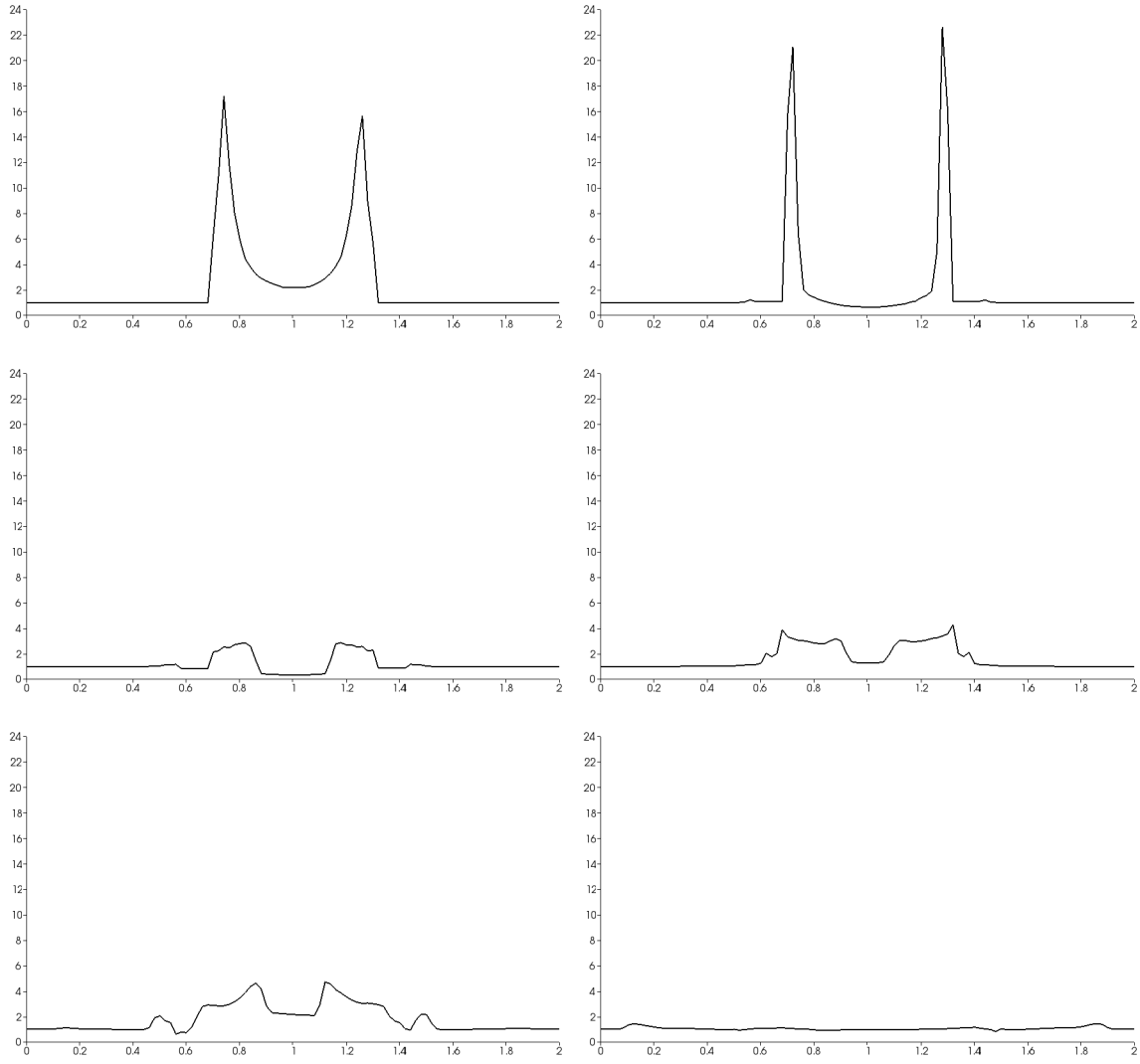


Figure 23: Pressure distribution along the line $\{x = 1.3, z = 1\}$ m at times 0.07s, 0.1s, 0.14s, 0.3s, 0.6s, and 0.9s from left to right and from top to bottom.

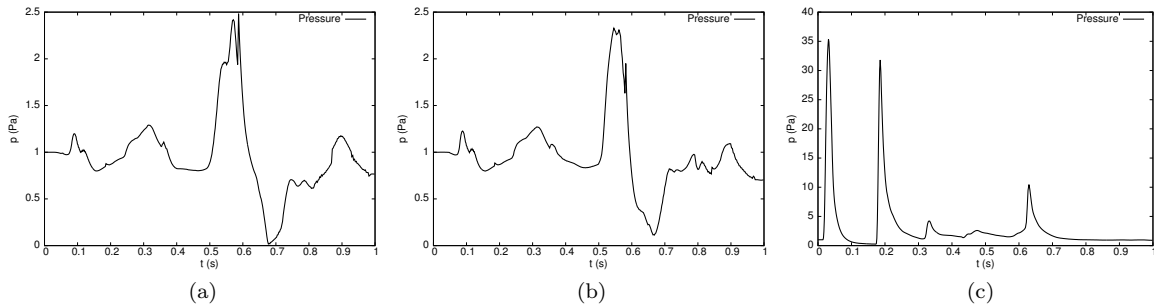


Figure 24: Evolution of the pressure in the cells containing (a) the point $(1.3, 1.4, 1)$ m, (b) the point $(1.3, 0.6, 1)$ m, and (c) the point $(1.3, 1, 1)$ m.

Acknowledgement This work was supported in part by CEA/DAM.

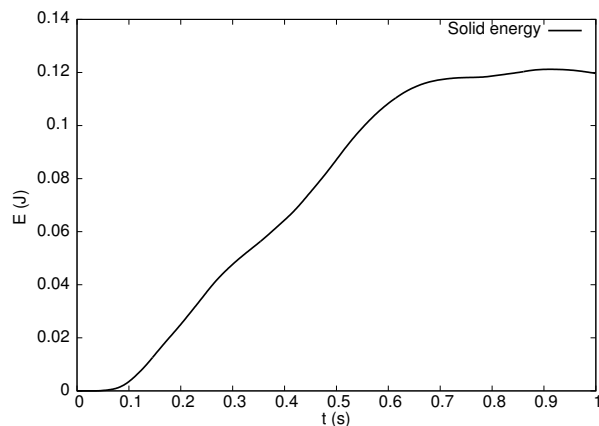


Figure 25: Time evolution of the solid energy.

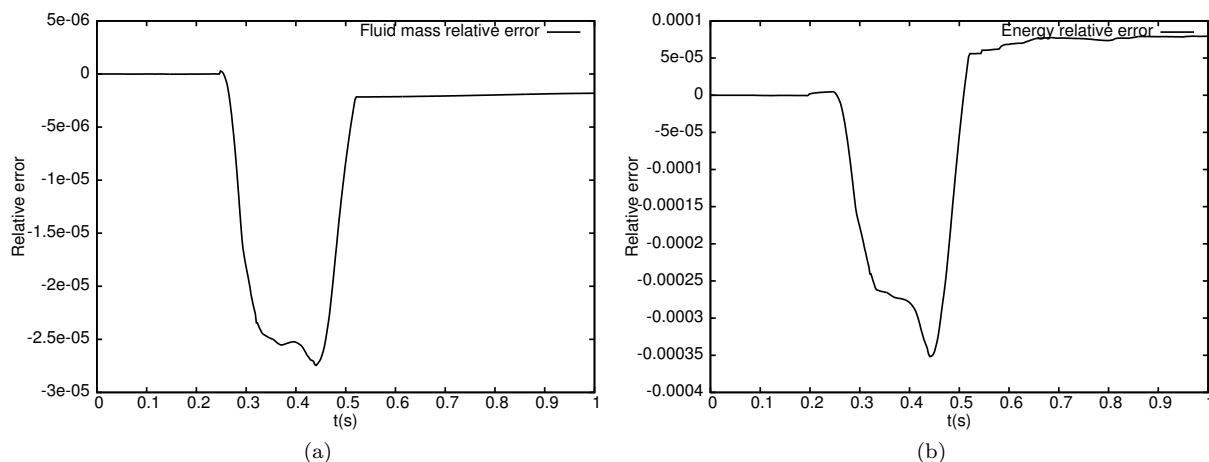


Figure 26: Relative conservation error on (a) fluid mass and (b) system energy.

REFERENCES

- [1] G. T. Camacho and M. Ortiz. Computational modelling of impact damage in brittle materials. *Int. J. Solids Structures*, 33(20):2899–2938, 1996.
- [2] F. Cirak, R. Deiterding, and S. P. Mauch. Large-scale fluid–structure interaction simulation of viscoplastic and fracturing thin-shells subjected to shocks and detonations. *Computers & Structures*, 85(11):1049–1065, 2007.
- [3] P. Colella, D. T. Graves, B. J. Keen, and D. Modiano. A Cartesian grid embedded boundary method for hyperbolic conservation laws. *J. Comput. Phys.*, 211(1):347–366, 2006.
- [4] V. Daru and C. Tenaud. High order one-step monotonicity-preserving schemes for unsteady compressible flow calculations. *J. Comput. Phys.*, 193(2):563–594, 2004.
- [5] P. De Palma, M. D. De Tullio, G. Pascazio, and M. Napolitano. An immersed-boundary method for compressible viscous flows. *Computers & fluids*, 35(7):693–702, 2006.
- [6] R. Deiterding, F. Cirak, and S. P. Mauch. Efficient Fluid-Structure Interaction Simulation of Viscoplastic and Fracturing Thin-Shells Subjected to Underwater Shock Loading. *International Workshop on Fluid-Structure Interaction*, page 65, 2009.
- [7] C. Denoual, G. Barbier, and F. Hild. A probabilistic approach for fragmentation of brittle materials under dynamic loading. *Comptes Rendus de l’Académie des Sciences-Series IIB-Mechanics-Physics-Chemistry-Astronomy*, 325(12):685–691, 1997.
- [8] J. Dolbow, N. Moës, and T. Belytschko. An extended finite element method for modeling crack growth with frictional contact. *Comput. Methods Appl. Mech. Eng.*, 190(51):6825–6846, 2001.
- [9] J. Donea, S. Giuliani, and J. P. Halleux. An arbitrary Lagrangian-Eulerian finite element method for

- transient dynamic fluid-structure interactions. *Comput. Methods Appl. Mech. Eng.*, 33(1):689–723, 1982.
- [10] D. Doyen, A. Ern, and S. Piperno. Quasi-explicit time-integration schemes for dynamic fracture with set-valued cohesive zone models. *Comput. Mech.*, 52(2):401–416, 2013.
- [11] Z. Dragojlovic, F. Najmabadi, and M. Day. An embedded boundary method for viscous, conducting compressible flow. *J. Comput. Phys.*, 216(1):37–51, 2006.
- [12] E. A Fadlun, R. Verzicco, P. Orlandi, and J. Mohd-Yusof. Combined immersed-boundary finite-difference methods for three-dimensional complex flow simulations. *J. Comput. Phys.*, 161(1):35–60, 2000.
- [13] J. Falcovitz, G. Alfandary, and G. Hanoch. A two-dimensional conservation laws scheme for compressible flows with moving boundaries. *J. Comput. Phys.*, 138(1):83–102, 1997.
- [14] C. Farhat, A. Rallu, and S. Shankaran. A higher-order generalized ghost fluid method for the poor for the three-dimensional two-phase flow computation of underwater implosions. *J. Comput. Phys.*, 227(16):7674–7700, 2008.
- [15] R. P. Fedkiw. Coupling an Eulerian fluid calculation to a Lagrangian solid calculation with the ghost fluid method. *J. Comput. Phys.*, 175(1):200–224, 2002.
- [16] A. A. Griffith. VI. The Phenomena of Rupture and Flow in Solids. *Phil. Trans. Roy. Soc.(Lon.) A*, 221:163–198, 1920.
- [17] D. Hartmann, M. Meinke, and W. Schröder. A strictly conservative Cartesian cut-cell method for compressible viscous flows on adaptive grids. *Comput. Methods Appl. Mech. Eng.*, 200(9):1038–1052, 2011.
- [18] X. Y Hu, B. C. Khoo, N. A. Adams, and F. L. Huang. A conservative interface method for compressible flows. *J. Comput. Phys.*, 219(2):553–578, 2006.
- [19] P. Le Tallec and J. Mouro. Fluid structure interaction with large structural displacements. *Comput. Methods Appl. Mech. Eng.*, 190(24):3039–3067, 2001.
- [20] P. D. Lea. *Fluid Structure Interaction with Applications in Structural Failure*. PhD thesis, Northwestern University, 2013.
- [21] R. J. LeVeque. *Finite volume methods for hyperbolic problems*, volume 31. Cambridge university press, 2002.
- [22] C. Mariotti and L. Monasse. *From general mechanics to discontinuity, unified approach to elasticity*. Presses des Ponts, 2012.
- [23] V. Michaut. Modeling of the dynamic fragmentation using a discrete element method/ Modélisation de la fragmentation dynamique par la méthode des éléments discrets. *PhD thesis, Ecole Centrale Paris, France*, 2011.
- [24] L. Monasse, V. Daru, C. Mariotti, S. Piperno, and C. Tenaud. A conservative coupling algorithm between a compressible flow and a rigid body using an Embedded Boundary method. *J. Comput. Phys.*, 231(7):2977–2994, 2012.
- [25] L. Monasse and C. Mariotti. An energy-preserving Discrete Element Method for elastodynamics. *ESAIM, Math. Model. Numer. Anal.*, 46:1527–1553, 2012.
- [26] R. B. Pember, J. B. Bell, P. Colella, W. Y. Crutchfield, and M. L. Welcome. An adaptive Cartesian grid method for unsteady compressible flow in irregular regions. *J. Comput. Phys.*, 120(2):278–304, 1995.
- [27] C. S. Peskin. Numerical analysis of blood flow in the heart. *J. Comput. Phys.*, 25(3):220–252, 1977.
- [28] M. A. Puscas, V. Daru, A. Ern, C. Mariotti, L. Monasse, and C. Tenaud. Conservative coupling method between an inviscid compressible flow and a deformable structure. *Submitted, <http://hal.archives-ouvertes.fr/hal-00993324>*, 2014.
- [29] M. A. Puscas and L. Monasse. A three-dimensional conservative coupling method between an inviscid compressible flow and a moving rigid solid. *Submitted, <http://hal.archives-ouvertes.fr/hal-00974602>*, 2014.
- [30] T. Rabczuk, R. Gracie, J.-H. Song, and T. Belytschko. Immersed particle method for fluid–structure interaction. *Int. J. Numer. Methods Engineering*, 81(1):48–71, 2010.
- [31] P. Schwartz, M. Barad, P. Colella, and T. Ligocki. A Cartesian grid embedded boundary method for the heat equation and Poisson’s equation in three dimensions. *J. Comput. Phys.*, 211(2):531–550, 2006.
- [32] G. Strang. On the construction and comparison of difference schemes. *SIAM Journal Numer. Anal.*, 5(3):506–517, 1968.
- [33] N. Sukumar and T. Belytschko. Arbitrary branched and intersecting cracks with the extended finite

- element method. *Int. J. Numer. Meth. Eng.*, 48:1741–1760, 2000.
- [34] J. W. Swegle and S. W. Attaway. On the feasibility of using smoothed particle hydrodynamics for underwater explosion calculations. *Comput. Mech.*, 17(3):151–168, 1995.
- [35] E. F. Toro. *Riemann solvers and numerical methods for fluid dynamics*, volume 16. Springer, 1999.
- [36] Y. H. Tseng and J. H. Ferziger. A ghost-cell immersed boundary method for flow in complex geometry. *J. Comput. Phys.*, 192(2):593–623, 2003.